Cancer Cell

Article

Spatial epitope barcoding reveals clonal tumor patch behaviors

Graphical abstract

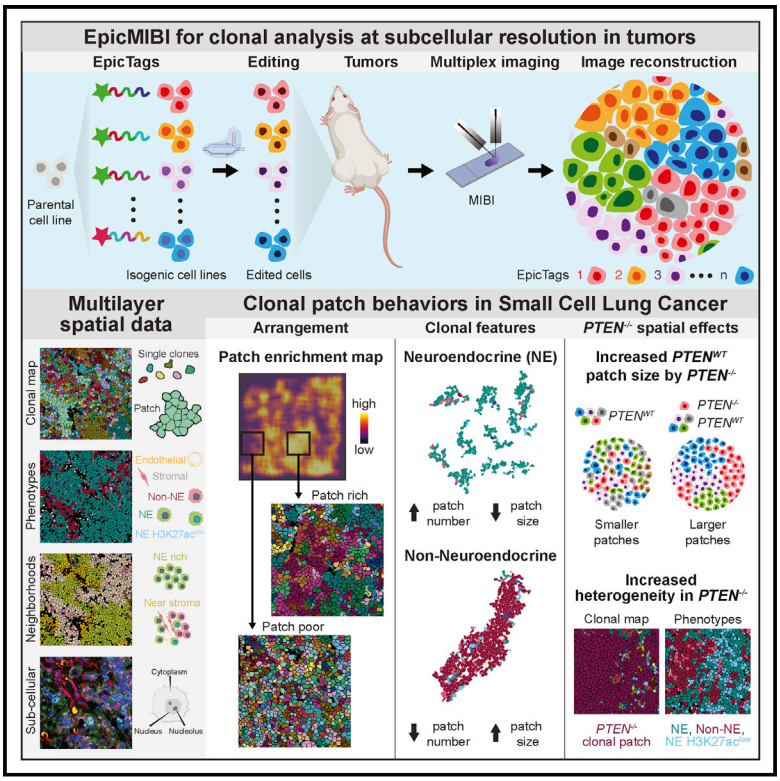

Highlights

- EpicTags enable *in situ* tracking of barcoded cells
- EpicMIBI provides spatial, cell-type, and cell-state depiction of clonal tumor patches
- Non-neuroendocrine cells display increased local clonal growth
- PTEN loss can promote a non-cell autonomous increase of clonal wild-type cell growth

Authors

Xavier Rovira-Clavé, Alexandros P. Drainas, Sizun Jiang, ..., Michael C. Bassik, Julien Sage, Garry P. Nolan

Correspondence

gnolan@stanford.edu (G.P.N.), julsage@stanford.edu (J.S.)

In brief

Rovira-Clave et al. employ a barcoding system and subcellular multiplex protein imaging to identify clonal behaviors in small cell lung cancer models. Non-neuroendocrine cells display increased local clonal growth compared with neuroendocrine cells. Loss of the *PTEN* tumor suppressor shifts tumor evolution through cell-intrinsic mechanisms and modifications on neighboring wild-type cells.

Rovira-Clavé et al., 2022, Cancer Cell *40*, 1423–1439
November 14, 2022
https://doi.org/10.1016/j.ccell.2022.09.014

CellPress

Cancer Cell

CellPress
OPEN ACCESS

Article

Spatial epitope barcoding reveals clonal tumor patch behaviors

Xavier Rovira-Clavé,[1,2,7] Alexandros P. Drainas,[3,4,7] Sizun Jiang,[1,5,7] Yunhao Bai,[1] Maya Baron,[3,4] Bokai Zhu,[1,2] Alec E. Dallas,[3,4] Myung Chang Lee,[3,4] Theresa P. Chu,[1] Alessandra Holzem,[3,4] Ramya Ayyagari,[3,4] Debadrita Bhattacharya,[3,4] Erin F. McCaffrey,[1] Noah F. Greenwald,[1] Maxim Markovic,[1] Garry L. Coles,[3,4] Michael Angelo,[1] Michael C. Bassik,[4] Julien Sage,[3,4,6,*] and Garry P. Nolan[1,6,8,*]

[1]Department of Pathology, Stanford University, Stanford, CA 94305, USA
[2]Department of Microbiology and Immunology, Stanford University, Stanford, CA 94305, USA
[3]Department of Pediatrics, Stanford University, Stanford, CA 94305, USA
[4]Department of Genetics, Stanford University, Stanford, CA 94305, USA
[5]Present address: Center for Virology and Vaccine Research, Beth Israel Deaconess Medical Center, Harvard Medical School, Boston, MA, USA
[6]Senior authors
[7]These authors contributed equally
[8]Lead contact
*Correspondence: gnolan@stanford.edu (G.P.N.), julsage@stanford.edu (J.S.)
https://doi.org/10.1016/j.ccell.2022.09.014

SUMMARY

Intratumoral heterogeneity is a seminal feature of human tumors contributing to tumor progression and response to treatment. Current technologies are still largely unsuitable to accurately track phenotypes and clonal evolution within tumors, especially in response to genetic manipulations. Here, we developed epitopes for imaging using combinatorial tagging (EpicTags), which we coupled to multiplexed ion beam imaging (EpicMIBI) for *in situ* tracking of barcodes within tissue microenvironments. Using EpicMIBI, we dissected the spatial component of cell lineages and phenotypes in xenograft models of small cell lung cancer. We observed emergent properties from mixed clones leading to the preferential expansion of clonal patches for both neuroendocrine and non-neuroendocrine cancer cell states in these models. In a tumor model harboring a fraction of PTEN-deficient cancer cells, we observed a non-autonomous increase of clonal patch size in *PTEN* wild-type cancer cells. EpicMIBI facilitates *in situ* interrogation of cell-intrinsic and cell-extrinsic processes involved in intratumoral heterogeneity.

INTRODUCTION

Heterogeneity within the cancer cell compartment of a tumor can be the result of genetic, epigenetic, and metabolic diversity, thus contributing to tumor progression and resistance to treatment (reviewed in [Easwaran et al. 2014; Jamal-Hanjani et al., 2015; Zahir et al., 2020; Hanahan and Weinberg 2011]). This heterogeneity begs essential questions: Do cancer clones behave largely autonomously, or do they functionally interact? Is the tumor simply a competition among related peers, or is there a social ecology of tumor cells with important contributory, symbiotic differences that must be present for success?

The recent development of multiplexed single-cell imaging technologies have added in-depth spatial characterization of cellular subtypes within tumors by simultaneously measuring dozens to hundreds of proteins or RNAs (Angelo et al., 2014; Eng et al., 2019; Rodriques et al., 2019; Goltsev et al., 2018; Schürch et al., 2020; Giesen et al., 2014; Chen et al., 2022; Liu et al., 2020). Multiplex ion beam imaging (MIBI), in particular, can capture post-translational modifications and measure over 40 proteins with a resolution down to 260 nm (Keren et al., 2019). MIBI is thus suitable to assess active and inactive proteins within their subcellular locales, while simultaneously revealing phenotypic, epigenetic, and metabolic cell states.

Complementarily, single-cell lineage tracing methodologies have been useful for delineating mutations that occur during cancer evolution (Kalhor et al., 2018; Bowling et al., 2020; Quinn et al., 2021). Adaptations to microscopy, such as the CRAINBOW system for fluorescently barcoding of somatic mutations, can provide snapshots of oncogenic clonal expansion *in vivo*, and its application suggests that tumor heterogeneity is not random but has some predetermined characteristics that are heritable (Boone et al., 2019). Previous work has adapted protein barcodes (Pro-Codes) for cancer cell tracking via antibody-based mass cytometry for high-dimensional single-cell CRISPR screens (Wroblewska et al., 2018). However, cell tracking methods are hampered by either absence of spatial resolution or limited parameters. Ideally, multiplexed single-cell imaging would be combined with lineage tracing to allow clonal and perturbation analysis of

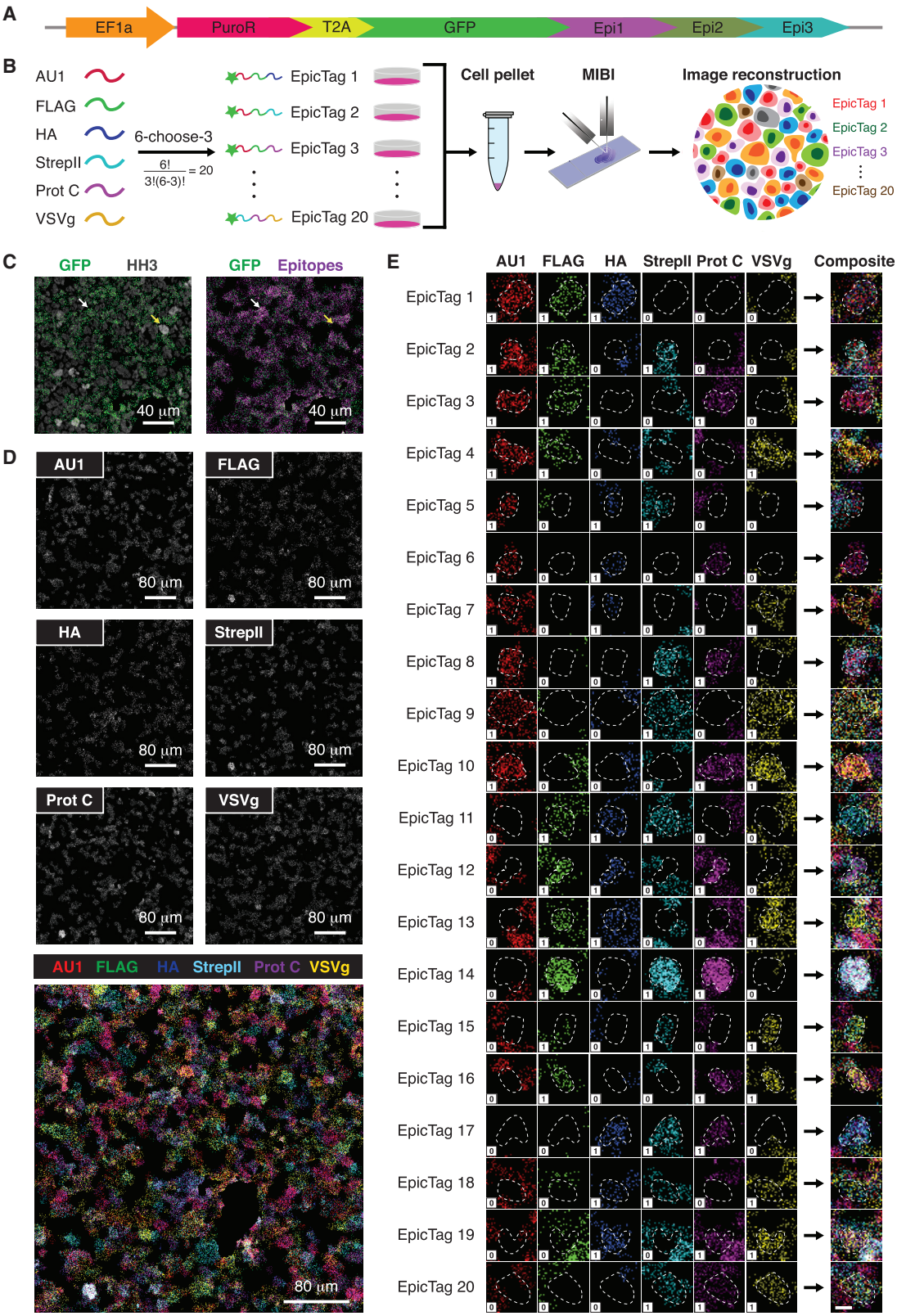

Figure 1. Imaging-based identification of specific cell populations with epitope-based barcodes

(A) Schematic of a representative EpicTag construct.

(B) Workflow for multiplex imaging of epitope-based barcodes in cell pellets.

(legend continued on next page)

individual cancer cells to the behavior and organization of the tumor microenvironment.

Here, we optimized Pro-Codes for multiparameter single-cell tissue imaging, which we named epitopes for imaging using combinatorial tagging (EpicTag), and coupled them with MIBI (EpicMIBI) for clonal growth tracking and the visualization of a snapshot of tumor evolution. Using xenograft models of small cell lung cancer (SCLC), an aggressive form of lung cancer with neuroendocrine (NE) features and considerable inter- and intratumoral heterogeneity (Simpson et al., 2020; Rudin et al., 2019; Gay et al., 2021; Groves et al., 2022), we found that homogeneously tagged cancer cells configure a tumor with reproducible phenotypically, epigenetically, and metabolically distinct cell types, with certain phenotypes attaining dominance within tumor patches. Importantly, an emergent structure is apparent dependence of co-localized phenotypes that create an ecosystem with NE and non-NE cancer cells arranging in defined cellular neighborhoods. We also observed that loss of the PTEN tumor suppressor can shift tumor evolution through cell-intrinsic mechanisms but also, in some contexts, by modifying behaviors of neighboring cancer cells that are *PTEN* wild-type. These results underscore the necessity of imaging approaches, such as EpicMIBI, to characterize the tumor microenvironment by delineating the individual contributions of cancer clones toward global tumor burden, with clear opportunities for novel anti-cancer therapies.

RESULTS

Imaging-based identification of cancer populations in tumors using epitope-based barcodes

To distinguish cell populations using epitope barcoding, we designed EpicTag vectors expressing a GFP reporter linked to a C-terminal tag consisting of combinations of epitopes (Figure 1A). We generated 20 NCI-H82 SCLC cell lines, each expressing three of six epitopes: AU1, FLAG, HA, StrepII, Prot C, and VSVg (Figure S1A). The 20 cell lines were then barcoded with a unique combination of palladium isotopes, pooled at the same ratio, and labeled with antibodies targeting GFP and the six epitopes. Mass cytometry showed GFP expression in the majority of the population and efficient detection of each of the epitope barcodes having unique palladium barcodes (Figures S1B–S1F), validating the 20 NCI-H82 barcoded cell lines.

Next, we used MIBI to distinguish barcoded cells in sections of cell pellets (Figure 1B). We generated a cell pellet consisting of 50% wild-type NCI-H82 cells and 50% of a pooled population of the 20 EpicTag-barcoded NCI-H82 cell lines. MIBI identified cells with and without GFP expression and expression of the epitopes was specifically detected in GFP$^+$ cells, as expected (Figure 1C). The analysis of signals for each of the epitopes revealed a multicolor image with all 20 barcodes (Figures 1D, 1E, and S1G). These *ex vivo* data indicate that antibody staining of epitope-tagged proteins, coupled to a multiplexed imaging technology, such as MIBI, enables the retention of spatial information for barcoded cells.

We next determined the potential of the EpicMIBI strategy *in vivo* by pooling the 20 barcoded cell lines to generate tumors in mice. All combinations of epitopes were again detected by mass cytometry in dissociated tumors (Figures S2A–S2D) and by MIBI on tumor sections (Figures 2A and 2B), indicating that EpicTag expression is durable *in vivo*. Thus, EpicMIBI can be leveraged as a proxy for common cell ancestry in proliferating murine tumors.

EpicTags are composed of a structured protein and a tail of epitopes. On the protein side, distinct proteins can be tagged with combinations of epitopes (Figure 2C, top). For example, we tagged mCherry with the six-choose-three ($^6C_3$) scheme described above and generated 20 additional mCherry$^+$ EpicTag-barcoded NCI-H82 cell lines (Figure S2E). We further validated the system by generating a pool excluding two cell lines and recovering the 38 expected combinations (Figure S2F). We then generated tumors in mice by mixing mCherry$^+$ and GFP$^+$ cancer cells and identified them by MIBI (Figures 2C and S2G). We further generated vectors expressing the E2 and Tag100 epitopes, grew tumors, and analyzed sections. We detected both epitopes *in vivo* and detected cells expressing up to six epitopes together and either GFP or mCherry (Figures 2D and 2E). Altogether, these experiments demonstrate the modularity and expandability of the EpicTag system through the diverse combination of well-expressed proteins tagged with a wide range of epitopes.

Complex spatial tumor structures arise from a well-established cancer cell line

NCI-H82 cells belong to the NEUROD1^{high} subtype of SCLC (SCLC-N) (Rudin et al., 2019). Similar to other SCLC subtypes, SCLC-N tumors are heterogeneous and harbor cancer cells with NE and non-NE features (Ireland et al., 2020; Stewart et al., 2020). Single-cell analyses suggested that cells with NE and non-NE features co-exist in NCI-H82 cells in culture (Lim et al., 2017; Groves et al., 2022). Accumulating evidence indicates that the interplay between NE and non-NE cells is critical for tumor growth and evolution in SCLC (reviewed in [Shue et al. 2018]).

We investigated the spatial organization of tumor heterogeneity in NCI-H82 xenografts using EpicMIBI, focusing on NE and non-NE phenotypes. We stained barcoded NCI-H82 tumors with an antibody panel to identify cell barcodes and various cell types in the tumor microenvironment and functional states for the cancer cells (Figure 3A). All the antibodies tested generated detectable signal with the expected cellular localization (Figure 3B). NCI-H82 cells were identified by GFP expression and further confirmed using a human-specific mitochondrial

(C–E) Representative MIBI images of a cell pellet. (C) Left: overlay of anti-GFP and anti-histone H3 (HH3) images showing GFP$^+$ (white arrow) and GFP$^-$ cells (yellow arrow). Right: overlay of anti-GFP and the sum of all six anti-epitope images. Scale bars, 40 μm. (D) Representative anti-epitope images from the same field of view (FOV). The multicolor overlay at the bottom shows that each GFP$^+$ cell expresses a combination of epitopes. Scale bars, 80 μm. (E) Multiple images showing a representative cell for each of the 20 barcodes. Dashed lines were manually drawn to indicate the contour of the relevant cell. The numbers within the white squares indicate whether the epitope was expected (1) or not (0). Images are enlargements from boxed regions in Figure S1G. Scale bars, 10 μm. See also Figure S1.

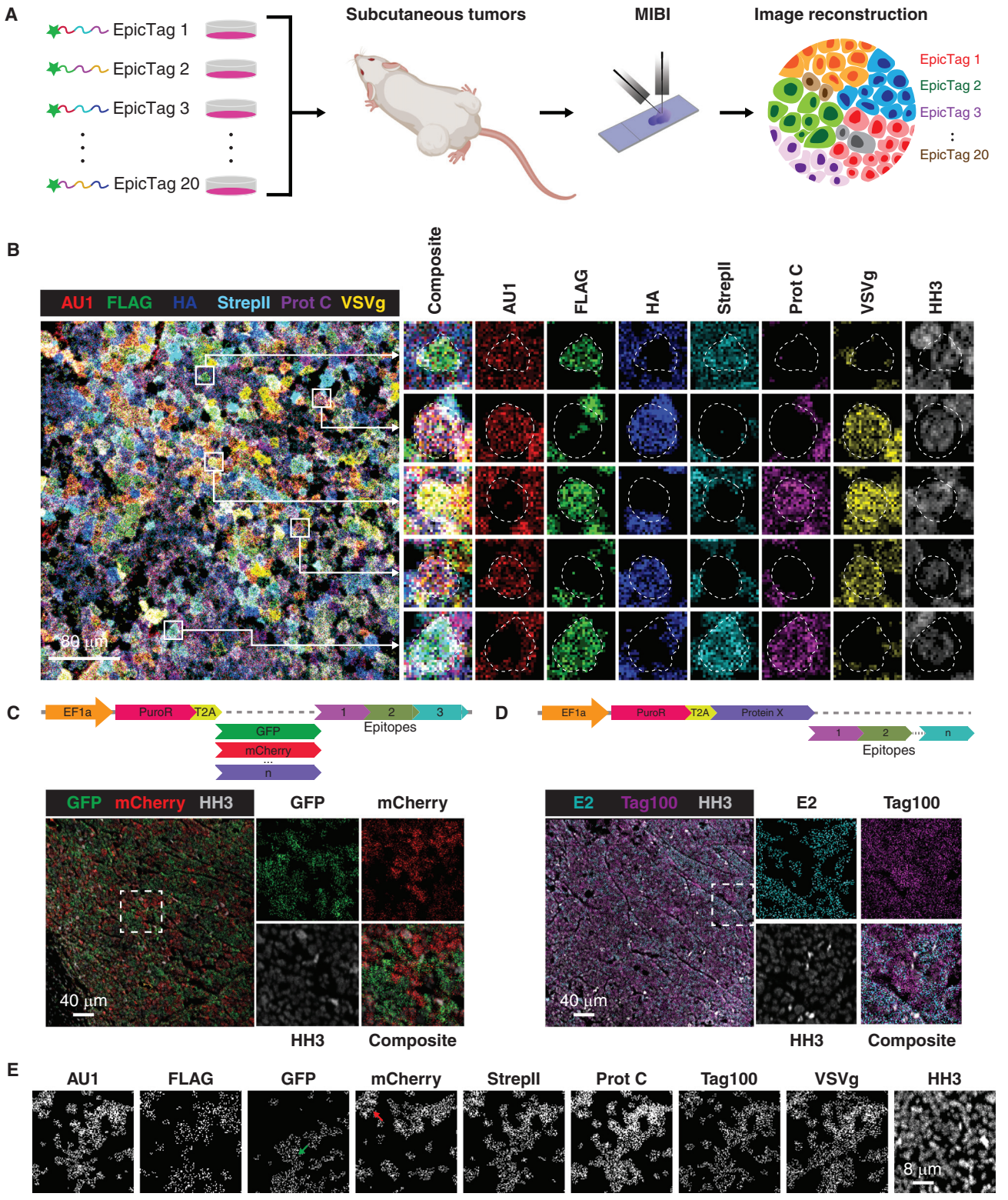

Figure 2. Detection of epitope-based barcodes in SCLC xenografts

(A) Workflow for multiplex imaging of epitope-based barcodes in subcutaneous NCI-H82 SCLC xenografts.

(B) Left: composite of anti-epitope images of a tumor consisting of a pooled population of 20 barcoded NCI-H82. Right: enlarged images from boxes in the left image showing that individual cells express three of the six epitopes. Scale bar, 80 μm.

(legend continued on next page)

marker (Figure 3C). For each NCI-H82 cell identified, barcode expression was analyzed, as well as markers of NE and non-NE differentiation (synaptophysin and vimentin, respectively), epigenetic states (H3K4me2, H3K27ac, and H4K8ac—histone modifications linked to active transcription), and metabolic states (GLUT1 and citrate synthase—markers for glycolysis and citric acid cycle activity, respectively) (Figure 3D). We also identified proliferative cells (Ki-67 and the mitosis marker phospho-Ser28 of histone H3, pS28 HH3) and cells with DNA damage (phospho-Ser139H2AX, γH2AX) (Figure 3E). In addition, we identified mouse endothelial (CD31) and stromal cells (α-smooth muscle actin [αSMA]) (Figure 3C). While the capabilities of the EpicTag system are illustrated here by a 22-antibody panel, this approach is also compatible with more extensive antibody panels (Figure S3A).

Overall, we analyzed 16 tiles from 6 tumors to obtain the spatial location and phenotype of >200,000 NCI-H82 SCLC cells (Figures S3B and S3C). Cell populations were defined using unsupervised self-organizing map (SOM) on the marker expression from all tiles. We identified eight phenotypic clusters: seven clusters based on SOM, and a final manual annotation step to identify $CD31^+$ cells (Figure 3F). Phenotypic clusters 2, 3, 5, 6, and 7 were of human origin, and clusters 1 and 4 were of mouse origin. Cluster 8, consisting of 0.7% of the total cells, contained cells with low levels of expression of all markers and it was removed from the analysis. Cluster 1 contained mouse stromal cells as indicated by the expression of αSMA and vimentin, and lack of expression of the human-specific mitochondrial marker. Cells in cluster 4 were mouse endothelial cells as indicated by the expression of CD31 and vimentin, and the absence of the human-specific mitochondrial marker. Non-NE NCI-H82 cells (marked by vimentin and absence of synaptophysin) were found in cluster 2, whereas NE cells (marked by synaptophysin and absence of vimentin) were split into clusters 6 and 7. The split into two NE clusters was mainly driven by differences in the expression of the epigenetic markers H3K27ac and H4K8ac, which were expressed in cluster 7 but not in cluster 6. Cluster 5 was composed of mitotic cells (marked by pS28 HH3). Cells in cluster 3 had high expression of both synaptophysin and vimentin. Visual inspection of cells in cluster 3 showed NE cells near stromal cells, suggestive of a leakage of signal from stromal cells into NE cells, even though some of these cells may also be transitioning between the NE and non-NE states (Figure S3D). GLUT1, citrate synthase, H3K4me2, Ki-67, and γH2AX were not informative for cluster annotation. Dimension reduction showed that cells from each phenotypic cluster grouped together (Figure 3G), supporting the clustering results.

We next calculated the frequencies of cells from each phenotypic cluster (Figure 3H) and mapped the localization of the clusters onto each tile (Figures 3I and S3E). Mouse stromal and endothelial cells (clusters 1 and 4, respectively) were present in all tiles analyzed (Figure 3H) and were scattered in the cluster-colored maps (Figure 3I). As expected for an NE cell line, more than 75% of the cells in all tiles combined were NE cells (clusters 6 and 7) (Figure 3H, "All tiles"), and these cells were also the major populations in each individual tile (Figure 3H). NE cells with high expression of H3K27ac (cluster 7) were a major population in all tiles (Figures 3H and 3I), whereas NE cells with low levels of expression of H3K27ac (cluster 6) were only present at a high frequency in a subset of tiles (Figures 3H and 3I; e.g., tile 15). Similarly, non-NE cells (cluster 2) were only present at a high frequency in some tiles (Figures 3H and 3I; e.g., tile 15). These results indicate that the distinct cancer cell states observed in NCI-H82 xenografts are not homogenously distributed, even within the same tumor.

In a reductionist view, if two phenotypes A and B are present in a tumor, they can be located in regions rich in A, rich in B, or containing both phenotypes (Figure 3J). Complexity escalates dramatically with increasing layered classifications. We previously showed that a tissue can be represented as a collection of cellular neighborhoods (CNs) (Schürch et al., 2020). The CN analytical framework defines regions of cells with a similar surrounding within tissues and enables a quantitative study of how cell location influence function. Phenotypes identified in the NCI-H82 xenografts were clustered based on their 30 nearest neighbors to obtain seven distinctive CNs (Figures 3K and S3F) that we mapped to the segmentation maps (Figures 3L and S3G). Certain CNs were enriched in cells with homotypic interactions: NE cells with high expression of H3K27ac (CN C), NE cells with low levels of H3K27ac ($H3K27ac^{low}$) (CN D), and non-NE cells (CN B) (Figures 3K and 3L). Other CNs were composed of several cell types and states. For example, CN A included NE and non-NE cells (Figures 3K and 3L). CN G, enriched in mouse cells, indicated vascularized and stromal regions of the tumor (Figures 3K and 3L). CN F was enriched in cells from cluster 3 ("double-positive cells"), suggesting that cells in this CN are surrounding the stroma (Figures 3K and 3L). CN E was composed of a mixture of NE cells with high and low expression of H3K27ac and non-NE cells (Figures 3K and 3L). Overall, 52.9% of cells within NCI-H82 xenografts were in CNs with homotypic interactions (CN B, C, and D). These analyses show that complex spatial rearrangements can arise *in vivo* even from a well-established cancer cell line, raising the question of whether clonal expansion of cancer cells drive the formation of such structures.

Clonal cancer cell growth is not spatially constrained to single patches in NCI-H82 xenografts

We reasoned that identifying the ancestries of the cells surrounding each cancer cell in NCI-H82 xenografts would provide insights into the processes that shape tumor architecture. By integrating cell- and pixel-based debarcoding approaches, we developed clonal tumor maps to represent the spatial location

(C–E) Representative MIBI images of a tumor consisting of a pooled population of wild-type NCI-H82 cells and four barcoded NCI-H82 cell lines expressing GFP or mCherry tagged to six epitopes (AU1, FLAG, StrepII, Prot C, Tag100, and VSVg) or to three epitopes (FLAG, HA, and E2). (C) Top: schematic of a representative EpicTag construct variable on protein expression. Bottom left: overlay of anti-GFP, anti-mCherry, and anti-HH3 images showing cells expressing GFP or mCherry but not both simultaneously. Bottom right: enlarged images from the box on the left. Scale bar, 40 μm. (D) Top: schematic of a representative EpicTag construct variable on the number of epitopes. Bottom left: overlay of anti-E2, anti-Tag100, and anti-HH3 images showing cells expressing Tag100 or E2 but not both simultaneously. Bottom right: enlarged images from the box on the left. Scale bar, 40 μm. (E) Images of the same FOV showing cells expressing either GFP (green arrow) or mCherry (red arrow) and six epitopes. Scale bar, 8 μm. See also Figure S2.

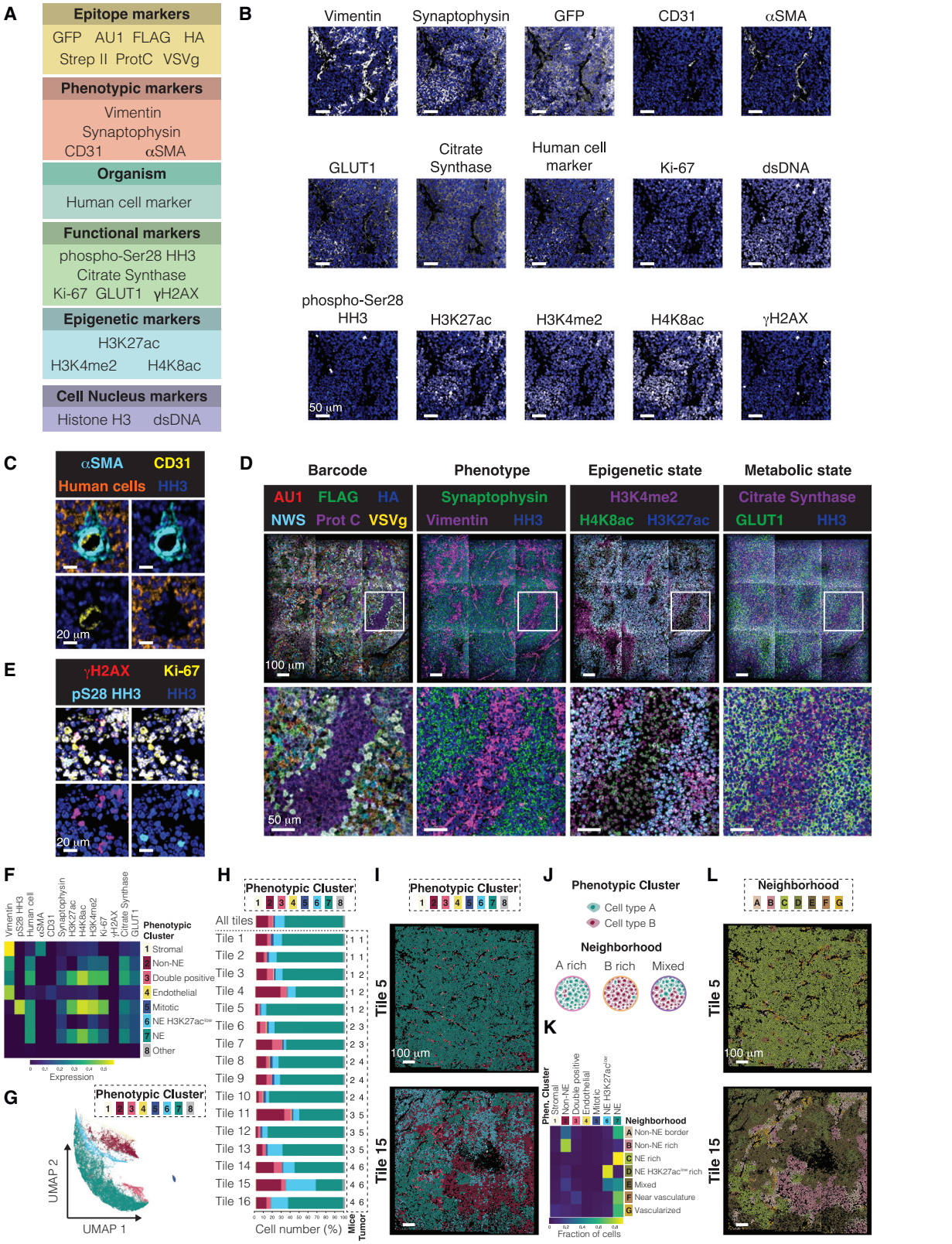

Figure 3. Spatial organization of NCI-H82 SCLC xenografts

(A) Summary of the antibody panel used for this study.

(B) Images for each marker in a representative region of an NCI-H82 xenograft. HH3 is shown in all images (blue). Scale bars, 50 μm.

(legend continued on next page)

of barcoded cells (Figure 4A and STAR methods). We identified the 20 possible epitope combinations in NCI-H82 xenografts using this pipeline (Figures 4B, 4C, and S4A), and both cell- and pixel-based debarcoding approaches identified all barcodes. Approximately 67% of the cells shared barcode in both approaches, indicating proper debarcoding accuracy (Figure S4B). The rest of cells were assessed for swapping from the cell- to pixel-based assignment to correct for mismatches and further improve debarcoding accuracy (STAR Methods). Some barcodes swapped at a higher frequency than others (Figure S4C) and the swap inversely correlated with patch size (Figure S4D), suggesting that proximity of certain epitope combinations in space is an important confounding effect, which is especially relevant for smaller clones. GFP and epitope expression correlated at the single-cell level (Figure S4E), which appears to be relevant for debarcoding, as cells with high barcode expression swapped less often than cells with low barcode expression (Figure S4F). Overall, each debarcoded cell line expressed the expected epitopes (Figure 4D), indicating that computational deconstruction of epitope-based images identifies common ancestries in the cancer cell population within the tumor.

We then debarcoded the NCI-H82 xenograft dataset to obtain a clonal tumor map for each tile (Figure S4G). After single-cell extraction and pooling, we obtained the percentages for each barcode (Figure 4E). The deviation from the expected 5% contribution from each of the 20 barcoded cell lines in some tiles and in the pool might be explained by several technical and biological issues, for instance minor differences at initial seeding (Figure S4H) and limited sampling. These data indicate that global tumor clonality is not a faithful representation of local clonal growth, suggesting that leveraging local scale as a variable may reveal novel mechanisms driving tumor evolution.

A clonal tumor map conveys a static and fractional picture of the local complexity of cell-cell interactions within a tumor. Despite these limitations, certain local cancer cell behaviors that shape tumor growth can be inferred in such clonal tumor map. Cancer cells sharing a barcode are expected to be detected both as individually distributed cells and as grouped in clonal tumor patches of distinct sizes (Figure 4F, top). Furthermore, individual cells and clonal tumor patches with the same barcode are expected both in proximity to one another and scattered through the tumor (Figure 4F, top). This distribution is expected to arise in concert with the distribution from other cancer cells with distinct barcodes (Figure 4F, top; gray cells). Individually distributed cells represented 33% of cancer cells in the NCI-H82 xenografts (Figure S4I); however, these cells could still be connected in the z axis to other cells with the same barcode. The remaining 67% were found within patches ranging in size from two cells to groups of hundreds of cells (Figure S4I). We plotted the distance of each cell with barcode 12 to the fifth nearest neighbor with the same barcode in tile 1 and observed that most distances were smaller than the ones from a randomized distribution (Figure S4J). The same trend appeared when considering the nearest neighbors up to 300 (Figure S4K) and was shared among all barcodes in all tiles in the dataset (Figure S4L). Together, these analyses show that cancer cells are not randomly distributed in NCI-H82 xenografts and tend to form clonal patches.

Spatial cell distribution within a tumor can be viewed as a grid of pairwise distances (Figure 4F, bottom). This representation summarizes all existing distances below a given threshold, revealing clonal dynamics otherwise difficult to observe. For all cells sharing the same barcode in a tile, we plotted the distances to the cells within the same patch and the distances to their nearest neighbors sharing a barcode. Some cancer cells sharing the same barcode grouped in relatively large, well-defined patches, whereas others were scattered individually around the tumor, far from cells of the same barcode. Certain patches co-existed near other patches of the same barcode (Figure 4G, top), and this spatial distribution did not occur in randomized data (Figure 4G, bottom). For each tile in the dataset, we applied a sliding window approach to quantify areas enriched in clonal patches higher than 10 cells. Certain areas of the tumor were enriched in individual cells and patches of a smaller size (Figure 4H; patch-poor) and certain others in patches of a larger size (Figure 4H; patch-rich). Notably, areas enriched in large patches were not only composed of one unique barcode but also of groups of patches with different barcodes (Figures S4G and S4M). These results indicate that clonal growth in NCI-H82 xenografts is not spatially constrained to single patches and is dependent on the local environment.

Non-NE SCLC cells establish large clonal patches within the tumor

Three basic layers of information can be extracted for each cell in the barcoded NCI-H82 xenograft dataset: the isogenic cell line to which the cell belongs (EpicTag barcodes), its type and state (phenotypic clusters), and the functional markers expressed (Figure 5A). The spatial component provides deeper layers of information on the cell type and state of the cells surrounding each

(C) Images for αSMA, CD31, and human cell marker in a representative region of the dataset. Scale bars, 20 μm.
(D) Images for 14 markers in a representative region of the dataset. These data exemplify antibody staining patterns used to assess barcode (left), phenotype (second to the left), epigenetic state (second to the right), and metabolic state (right). Scale bars, 100 μm (top) and 50 μm (bottom).
(E) Images of γH2AX, Ki-67, and pS28 HH3 in a representative region of the dataset. Scale bars, 20 μm.
(F) A heatmap of mean marker expression in the eight phenotypic clusters (rows). The intensity of each marker is defined by the color bar at the bottom (normalized counts). The mitotic phenotypic cluster is composed by non-NE and NE cells.
(G) UMAP of all cells in the dataset (n = 231,715) colored by their phenotypic cluster.
(H) Frequencies of each phenotypic cluster in the entire dataset (n = 231,715) and in each individual tile (tiles 1 to 16).
(I) Representative phenotypic cluster maps on a region enriched in NE cells (tile 5; phenotypic cluster 7) and a region with distinct cell types (tile 15; phenotypic clusters 1 to 8). Scale bars, 100 μm.
(J) Schematic of cellular neighborhoods.
(K) A heatmap of the frequencies of each phenotypic cluster for each of the seven CNs (rows).
(L) Representative neighborhood maps on a region enriched in homotypic NE cell interactions (tile 5; CN 3) and in a region with distinctive substructures (tile 15; CNs 1 to 7). Scale bars, 100 μm. See also Figure S3.

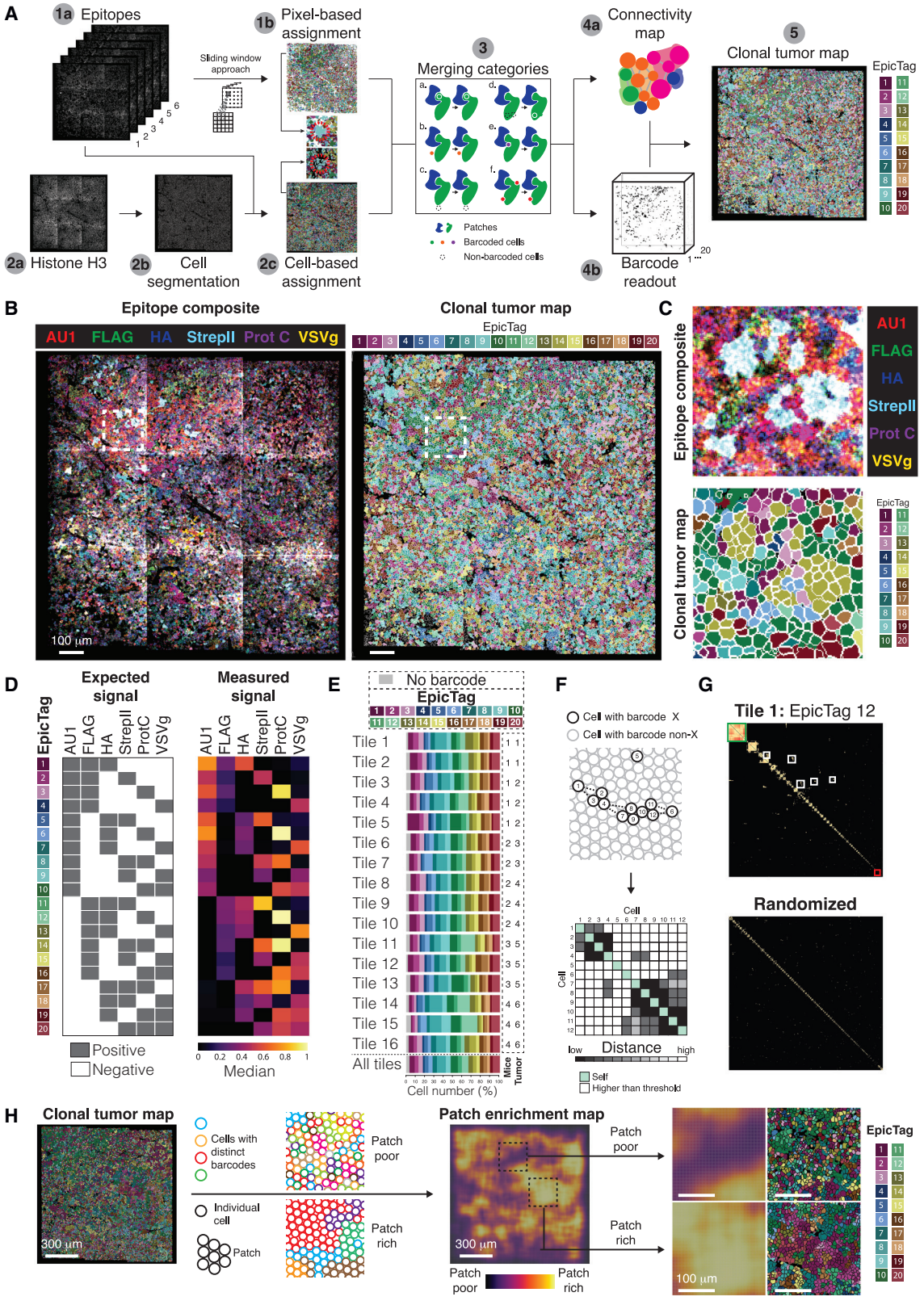

(legend on next page)

cell (i.e., the CN), inference of clonality of surrounding cancer cells (i.e., tumor patches), and the subcellular location of the markers (Figure 5A). For an integrative data visualization, we plotted the expression of eight markers for all barcoded cells from the non-NE, NE H3K27ac^{low}, and NE cell states (clusters 2, 6, and 7, respectively) in all CNs (Figure S5A). The coefficients of variation of marker expression among barcodes in each cancer cell state and CN (Figures S5B and S5C) indicate that there is an overall similar expression of markers across cancer cell states on the three main cancer cell states (non-NE, NE, and NE H3K27ac^{low}) in their respective homotypic CNs (Figure 5B) as well as outside the clusters in their homotypic CNs (Figure S5A), as would be expected for 20 isogenic cell lines and CNs, with rare exceptions that might be explained by the low number of cells analyzed. Taken together, these analyses show good marker expression agreement among barcodes across clusters and CNs.

EpicTag-barcoded NCI-H82 cells generate patches of a broad range of sizes. We asked whether the total number of cells correlated with increased patch numbers and sizes for each barcode and phenotypic cluster. For NE cells (cluster 7), the number of cells and patches strongly correlated across barcoded cell lines (R_{adj}^2 = 99%) (Figures 5C and S5D). In contrast, there was a lower correlation for non-NE cells (cluster 2; R_{adj}^2 = 63%) (Figures 5C and S5D). An exponential model might provide a better fit to the non-NE data (R_{adj}^2 = 84%) (Figure 5C), but few data points inform the curve. Although the data points are limited by the number of barcodes, these results suggest that the mechanisms of expansion differ for the NE and non-NE patches. The barcoded cells are from the same parent cell culture, and we expected similar barcode representations across the different clusters (with cells switching from one state to another similarly in all barcoded cell lines), which was observed for most phenotypic clusters (Figure S5E). One notable exception was the lack of correlation for the ratio between NE and non-NE cells (clusters 7 and 2, respectively) when comparing barcoded cell lines (Figure S5F), suggestive of specific dynamics in the acquisition of these cancer cell states within tumors.

The non-NE cells (cluster 2) generated fewer patches than the NE cells (cluster 7) (Figure 5C). The ratio of the slopes from the linear models indicates that, for NE cells (cluster 7), 1.8 times more cells were in fewer patches than for non-NE cells (cluster 2), suggesting that non-NE cells are contained in larger patches (Figure 5D, white arrow). Indeed, patch size was significantly larger in non-NE (cluster 2) compared with NE (cluster 7) and other cell states (Figures 5E, right, and S5G and H). These data suggest that NCI-H82 cells with a non-NE phenotype remain together after cell division and tend to form larger patches. Certain areas of the NCI-H82 xenografts are enriched in large patches of non-NE cells (cluster 2) from distinct isogenic cell lines (Figures S3E, e.g., tiles 4 and 14, and 5D). This is in contrast to other areas of the NCI-H82 xenografts, where non-NE cell (cluster 2) patches are mostly absent (Figure S3E, e.g., tiles 5 and 10). Close to the large patches of non-NE cells (cluster 2), other large patches of NE cells (cluster 7) sharing the same barcode are observed (Figure 5D, yellow arrows). This suggests that, in certain regions of the tumor, interactions of non-NE cells are stabilized, switching the phenotype of the tumor in that area to a non-NE phenotype.

Non-NE cells (cluster 2) were identified in all barcoded populations (Figure 5E), but six barcoded cell lines generated much larger patches of non-NE cells (cluster 2) compared with their NE counterparts (cluster 7) (Figure 5E; EpicTags 5, 6, 8, 12, 14, and 18) and four barcoded cell lines contained only 25–50 cells of non-NE cells (cluster 2) (Figure 5E; EpicTags 1, 3, 4, and 17), depicting a high variation in non-NE cell number across the 20 barcoded cell lines. Notably, approximately 90% of cells in each patch were assigned to the same cluster and the presence of a dominant cluster was significantly higher than expected based on a random distribution (Figure S5I). These observations suggest that NCI-H82 cells grown *in vivo* are mostly NE in nature but that large patches of non-NE cells may sometimes "stabilize" and expand in response to unknown stimuli.

We surmised that the generation of these large patches of non-NE cells (cluster 2) may be due to increased proliferation. Analysis of Ki-67, a marker of non-quiescent cells (Miller et al., 2018), showed that mitotic cells (cluster 5) had the highest level of Ki-67 expression (Figure 5F), as expected. In non-NE cells (cluster 2), Ki-67 levels significantly increased, and the number of quiescent cells significantly decreased with patch size (Figures 5F and 5G). In contrast, there was no significant correlation between Ki-67 expression, number of quiescent cells, and patch size for NE cells (cluster 7) (Figures 5F and 5G). NE H3K27ac^{low} cells (cluster 6) had a low proliferative index (Figures 5F and 5G), highlighting a functional difference with NE cells (cluster 7). Interestingly, non-NE (cluster 2) and NE cells

Figure 4. A debarcoding strategy identifies clonal tumor patches

(A) Pipeline to reconstruct clonal tumor maps.

(B and C) Representative clonal tumor map from a barcoded NCI-H82 xenograft. (B) Left: overlay of anti-epitope images. Right: clonal tumor map of the image on the left. Scale bars, 100 μm. (C) Enlarged view of the white boxes in (B).

(D) Epitope signal on each debarcoded population. Left: expected signal for each epitope in each barcode. Gray indicates positive signal. Right: measured epitope signal in each debarcoded population from (B). Color shows the median of the normalized counts.

(E) Frequencies of each EpicTag barcode in the dataset (n = 231,715) and in each individual tile (tiles 1 to 16).

(F) Top: schematic representation of cells with the same EpicTag barcode. Cells with a particular barcode can be individually distributed (e.g., cell 1) or grouped (e.g., cells 2 to 4). Cells sharing a barcode can be distributed nearby (e.g., cells 6 and 11) or far apart (e.g., cell 5). Bottom: schematic grid of pairwise distances of the schematic shown on top.

(G) Grid of pairwise interactions showing the distances of each cell to its fifth nearest neighbor for cells with EpicTag 12 in tile 1 (top) and a randomized sample (bottom). Randomization was performed by randomly assigning EpicTag 12 to segmented cells in tile 1, up to the number of EpicTag 12 in tile 1. Cells were arranged in the diagonal by patch size (larger patches in the top left corner). The green box exemplifies a clonal tumor patch. The white boxes exemplify clonal tumor patches that are closer in space. The red box exemplifies individually scattered cells.

(H) A clonal tumor map (left image) can be decomposed based on the size of the clones into patch enrichment maps (middle image). Certain areas are enriched in patches (right, bottom image) or depleted (right, top image). See also Figure S4.

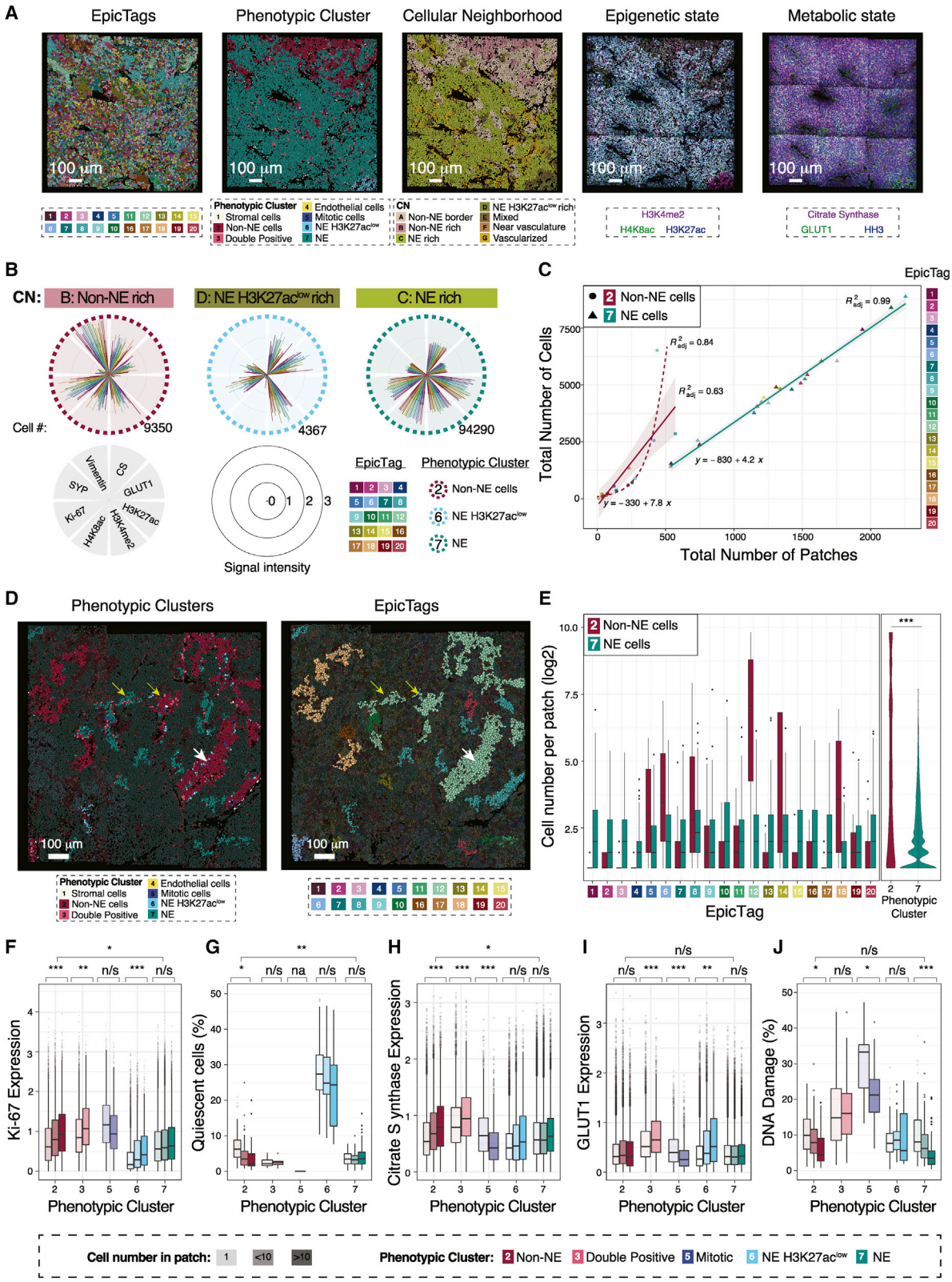

Figure 5. Non-neuroendocrine SCLC cells establish large patches with increased proliferative index and decreased DNA damage

(A) Overview of the different layers obtained with epicMIBI. Scale bars, 100 µm.

(B) Polar plots of marker expression in homotypic CNs (cluster 2, CN B; cluster 6, CN D; cluster 7, CN C). Synaptophysin (SYP) and citrate synthase (CS).

(legend continued on next page)

(cluster 7) were more quiescent in CN D (18% and 11%, respectively), which is enriched in NE H3K27ac^{low} cells (cluster 6) (Figures S5J and S5K). This suggests that the proliferation of NE and non-NE cells is affected by the presence of more slowly cycling NE-H3K27ac^{low} cells. Ki-67 expression was higher in the larger patches across all CNs, although this was observed to a less extent for CN D, enriched in NE H3K27ac^{low} cells (cluster 6) (Figure S5L). Notably, citrate synthase expression was significantly elevated in larger non-NE (cluster 2) patches (more than 10 cells), but GLUT1 levels were similar across patch sizes in both non-NE (cluster 2) and NE cells (cluster 7) (Figures 5H and 5I), suggesting elevated activity of the citric acid cycle compared with glycolysis in larger non-NE patches. Finally, we noted that that larger patches (more than 10 cells) of non-NE (cluster 2) and NE cells (cluster 7) showed less DNA damage (Figure 5J) independent of the neighborhood in which these cells were located (Figure S5M). Decreased DNA damage, changes in metabolism, and increased proliferation may all contribute to the expansion of larger non-NE clonal patches once small patches have formed.

Our results are influenced by the choice of antibodies in the panel. NEUROD1 is highly expressed in NCI-H82 cells; NOTCH2 and YAP1 are non-NE markers in SCLC (Tlemsani et al., 2020; Lim et al., 2017; Shue et al., 2022). While these antibodies were not included in our epicMIBI panel, single staining showed widespread expression of NEUROD1 throughout the tumor, as expected, but distinctive patch-like staining for NOTCH2 and YAP1 (Figure S5N), reminiscent of the pattern observed for vimentin.

PTEN loss in the NCI-H82 model promotes a non-cell autonomous increase of patch size in neighboring *PTEN* wild-type cancer cells

PTEN is a known tumor suppressor in SCLC (McFadden et al., 2014; Cui et al., 2014), but the evolution of *PTEN* mutant clones within SCLC tumors has not been examined. We knocked out *PTEN* by Cas9-sgRNA ribonucleoprotein (RNP) delivery (*PTEN*$^{-/-}$) in NCI-H82 cells expressing EpicTags 1 and 20 and generated six control cell lines (EpicTags 2, 4, 14, 16, 17, and 18) by delivering non-targeting RNPs (Figure 6A). These 8 cell lines were then pooled with the remaining 12 wild-type EpicTag-barcoded NCI-H82 lines to generate a population consisting of 20 cell lines ("*PTEN*$^{-/-}$ pool"), and a pool of the 20 original EpicTag-barcoded lines was used as a control. In the *PTEN*$^{-/-}$ pool, EpicTag lines 1 and 20 grew more rapidly in culture than the other lines (Figures 6B and 6C), as assessed by mass cytometry, and accounted at the end of the experiment for 15% and 29% of the population, respectively. The original (*PTEN* wild-type) EpicTag lines 1 and 20 did not have a competitive advantage (Figure 6C). These observations validated the expected tumor suppressor role for *PTEN* in SCLC cells in culture.

We next analyzed by MIBI >198,000 cells from ten tiles from tumors generated from the *PTEN*$^{-/-}$ pool and four tiles from tumors with only *PTEN* wild-type cells. All 20 barcodes were detected in tumors from both groups (Figure S6A). Surprisingly, in this context, *PTEN*$^{-/-}$ cells did not expand more than control cells (Figure 6C, right). We also found no difference in the proliferation of *PTEN*$^{-/-}$ and control cells in the xenografts (Figure S6B). These data show that *PTEN* knockout in NCI-H82 cells provides a competitive growth advantage in culture but not *in vivo* in the context studied, suggesting that wild-type and *PTEN*$^{-/-}$ cells may interact differently in 3D tumors than *in vitro*. However, the overall tumor architecture, as defined by SOM clusters and CNs, was comparable between pools containing *PTEN*$^{-/-}$ cells and controls (*PTEN* wild-type) (Figures S6C–S6G), suggesting that no major differences in the spatial arrangements of the NCI-H82 xenografts were induced when 10% of the population lacked PTEN.

We next analyzed patches in tumors generated from the *PTEN*$^{-/-}$ pool and in tumors from the *PTEN* wild-type pool. Similar to our previous analysis (Figure S5I), we observed patches of cells with a dominant phenotype for the control (*PTEN* wild-type) cells (Figure S6H). In contrast, the patches of cells that lacked *PTEN* were generally composed of multiple cell states (Figure S6H), including patches with a mixture of NE (cluster 7), vimentin^{+} (cluster 2), and NE H3K27ac^{low} (cluster 6) cells (Figure S6I). Notably, *PTEN*$^{-/-}$ cells had a higher percentage of NE H3K27ac^{low} cells (cluster 6) compared with control cells in the same tumor (Figure 6D). NE H3K27ac^{low} cells (cluster 6) were smaller than conventional NE cells (cluster 7) (Figure S6J) and were identified in areas with features of necrosis (Figure S6K). In pellets from *in vitro* cultured *PTEN*$^{-/-}$ and control (*PTEN* wild-type) NCI-H82 cells, *PTEN*$^{-/-}$ cells had higher vimentin expression, similar H3K27ac expression, and similar levels of cell death compared with control cells (Figure S6L). In NCI-H82 xenografts, *PTEN*$^{-/-}$ cells were more likely to be in CN E (Figure 6E), areas of the tumor corresponding to the border between regions rich in conventional NE cells (cluster 7) and NE H3K27ac^{low} (cluster 6) (Figure 6F). Cells in CN E expressed considerably less H3K27ac compared with cells in CN C, and levels of H4K8ac were lower than in CN C and CN D, although the difference was less dramatic (Figure S6M), suggesting a stepwise process of epigenetic alterations. Overall, these data show that loss of *PTEN* in NCI-H82 cell populations *in vivo* is accompanied by a higher number of vimentin-positive cells (cluster 2) and NE H3K27ac^{low} cells (cluster 6) as well as co-residence of these cell types with NE cells (cluster 7) within the same clonal tumor patch, which may account for the lack of observed competitive advantage of *PTEN*$^{-/-}$ cells *in vivo*.

(C) Total number of barcoded cells and patches for each EpicTag plotted for clusters 2 (non-NE) and 7 (NE) in all acquired tiles.
(D) Representative image of large patches with phenotypic clusters and EpicTag barcodes indicated. White arrow highlights a large patch of non-NE cells. Yellow arrows indicate where non-NE and NE cells share the same barcode. Scale bars, 100 μm.
(E) Patch sizes by cell number per EpicTag for cluster 2 (non-NE cells, red) and cluster 7 (NE cells, green). $p = 2.2*10^{-16}$.
(F–J) Single-cell analysis in individual clusters. For each cluster the data were separated by patch size: 1 cell, 1 to 10 cells, and over 10 cells. Significance is calculated by ANOVA within and between groups and adjusted by Bonferroni (Table S1). *p-adj = 0.05–0.01, **p-adj = 0.01–0.001, ***p-adj < 0.001. (F) Ki-67 expression. (G) Quiescent cells per cluster quantified by the percentage of cells per cluster that are negative for Ki-67 expression. (H) Citrate synthase expression. (I) GLUT1 expression. (J) Percentage of cells with DNA damage per cluster, inferred from γH2AX expression. See also Figure S5.

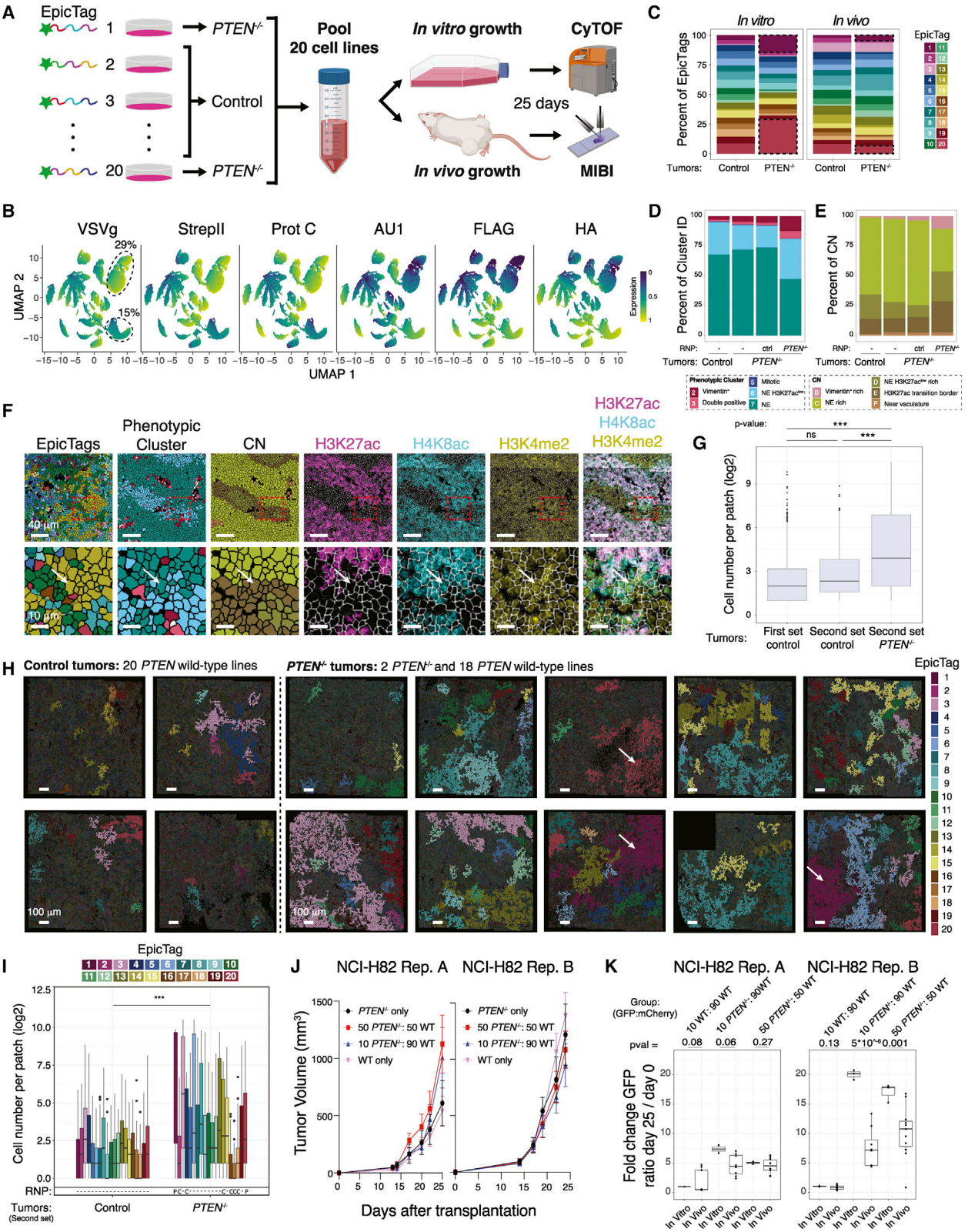

(legend on next page)

Our patch analysis of control NCI-H82 xenografts (Figure 4) provided a ground truth for the expected clonal growth dynamics of this cell line *in vivo* (Figure 6G; "First set control"). The same patch size was also observed in the control tumors generated in parallel to the tumors containing *PTEN*$^{-/-}$ populations (Figure 6G; "Second set control"). Strikingly, the clonal patches were larger in tumors containing *PTEN*$^{-/-}$ cells than in tumors with only control cell lines (Figure 6G; "Second set *PTEN*$^{-/-}$"). Not only were patches containing *PTEN*$^{-/-}$ cells larger, but there was also an increase of patch size for most *PTEN* wild-type control cell lines (Figures 6H and 6I). Larger patch size in control cells in tumors containing *PTEN*$^{-/-}$ cells could not be explained by increased proliferation, altered GLUT1 or citrate synthase levels, higher amounts of DNA damage, or total tumor size (Figures S6N–S6P). While the reason for the larger patch size remains unknown, and was unexpected, these data demonstrate that the overall architecture of NCI-H82 xenografts is altered by the presence of a *PTEN*$^{-/-}$ population seeded at ~10%.

We measured tumor growth in mice after transplant of samples containing defined ratios of control and *PTEN*$^{-/-}$ cells and observed that the presence of *PTEN*$^{-/-}$ cells did not influence tumor size (Figure 6J). Furthermore, the ratio of *PTEN*$^{-/-}$ to wild-type *PTEN* control cells was higher *in vitro* than *in vivo* (Figure 6K), and tumor size was not greater in mice transplanted with a higher percentage of *PTEN*$^{-/-}$ cells (Figure S6Q). These tumor growth measurements further support our hypothesis that cancer cell-intrinsic, pro-growth phenotypes, such as those induced by *PTEN* loss, can be reshaped by the tumor microenvironment. In NCI-H82 xenografts, the modified tumor architecture is not just explained from a *PTEN*$^{-/-}$ cell-intrinsic perspective: these genetically edited cells exert non-autonomous effects on other cancer cells within the tumor.

We further validated the EpicMIBI approach and examined some of the key finding of the NCI-H82 model using NJH29 cells, another SCLC-N model. We grew tumors containing defined ratios of control and *PTEN*$^{-/-}$ NJH29 cells and observed that tumors with only *PTEN*$^{-/-}$ cells had some growth advantage (Figure S7A). We quantified the percentage of each barcode in the tumors from the mixed and control pools by EpicMIBI and analyzed cells grown *in vitro* by CyTOF. *In vivo*, we analyzed >287,000 cells from 8 mixed tumors and 7 control tumors (Figure S7B). Cells in the control pool grew at similar rates both *in vitro* and *in vivo* (Figure S7C), validating the experimental approach. Missing barcodes had the fewest counts with a false positive rate of 0.01% *in vitro* and 1.5% *in vivo* (Figure S7C), validating the debarcoding approach. *PTEN*$^{-/-}$ cells in the mixed pool accounted for a total of 83% of the population *in vitro*, and 38% of the population *in vivo* (Figure S7C). As also observed in the NCI-H82 model, *PTEN*$^{-/-}$ NJH29 cells expanded less *in vivo* than *in vitro* (Figures S7C and S7D). Interestingly, *PTEN*$^{-/-}$ NJH29 cells and wild-type NJH29 cells in mixed tumors proliferated *in vivo* at a similar ratio than cells in control tumors (Figure S7E). Overall, these results show that PTEN is a strong tumor suppressor *in vitro* in the NJH29 cell model, but its loss only leads to limited increased tumor growth *in vivo*.

PTEN$^{-/-}$ NJH29 cells arranged in large clonal patches, as observed in the NCI-H82 model (Figures S7F and S7G). In contrast to the NCI-H82 model, however, the clonal *PTEN* wild-type patches were not larger in tumors containing *PTEN*$^{-/-}$ cells than in tumors with only control cell lines (Figures S7F and S7G). The phenotypic clusters and their percentages observed in control NCI-H82 xenografts were conserved in control NJH29 xenografts (Figure S7H-K), but the overall spatial distribution was shifted toward increased intermixing of NE-H3K27ac^{low} cells (cluster 6) with NE cells (cluster 7) (Figures S7L–S7N). Similar to the observation made in NCI-H82 xenografts, NE H3K27ac^{low} NJH29 cells (cluster 6) were smaller than NE cells (cluster 7) (Figure S7O), suggesting that these two NE clusters are functionally distinct in the two models. *PTEN*$^{-/-}$ NJH29 cells had a higher percentage of non-NE cells (cluster 2) but not NE H3K27ac^{low} cells (cluster 6) compared with the wild-type cells within the same tumor (Figure S7J). As also observed in NCI-H82 xenografts, patches of NJH29 cells that lacked *PTEN* were characteristically heterogeneous compared with *PTEN* wild-type patches in the same tumor and control tumors (Figure S7P).

In summary, PTEN is a potent tumor suppressor *in vitro* for both NCI-H82 and NJH29 cell lines and its loss leads to limited

Figure 6. PTEN deficiency in a fraction of cancer cells modifies tumor architecture through cell-intrinsic and -extrinsic mechanisms

(A) Workflow for multiplex imaging of genetically modified epitope-based barcoded cells in subcutaneous NCI-H82 xenografts.

(B) UMAP of cultured cells (n = 69,065) grouped and colored by epitope expression. Dashed ellipses and percentages indicate *PTEN*$^{-/-}$ EpicTag 1 (bottom) and 20 (top).

(C) Frequencies of each EpicTag barcode in cells grown *in vitro* and *in vivo* in "Control" and "*PTEN*$^{-/-}$" pools. Black dashed boxes indicate *PTEN*$^{-/-}$ cells.

(D) Frequencies of each phenotypic cluster in "Control" (n = 56,199) and "*PTEN*$^{-/-}$" (n = 142,056) tumors. For the "*PTEN*$^{-/-}$" tumors, frequencies for *PTEN* wild-type cells ("–"), *PTEN* unedited but nucleofected cells ("ctrl"), and *PTEN* knockout cells ("*PTEN*$^{-/-}$") are shown.

(E) Frequencies of each CN in "Control" and "*PTEN*$^{-/-}$" tumors.

(F) Clonal tumor, phenotypic cluster, and CN maps, and epigenetic markers in a representative region of a *PTEN*$^{-/-}$ NCI-H82 xenograft highlighting wild-type cells. Bottom row images are enlarged representations of red dashed squares in the top row. White arrows indicate representative H3K27ac^{-}, H4K8ac^{+}, and H3K4me2^{+} cells enriched in CN E. Scale bars, 40 μm (top) and 10 μm (bottom).

(G) Overall patch size by cell number in "Control" and "*PTEN*$^{-/-}$" tumors. The overall patch size from the dataset shown in Figure 5 is shown as reference ("First set control"). P values calculated by the Student's t test.

(H) Images of clonal tumor map with EpicTag barcodes highlighted in patches of more than 50 cells in "Control" and "*PTEN*$^{-/-}$" tumors. White arrows indicate *PTEN* knockout patches. The legend indicates the color for each EpicTag barcode. The black square in the image at the bottom, second from the right, is consequence of a tile having eight FOVs instead of nine (see Figure S3C). Scale bars, 100 μm.

(I) Patch size by cell number per EpicTag in "Control" and "*PTEN*$^{-/-}$" tumors. P value calculated by the Student's t test.

(J) Tumor volume of 25 days of growth in mice. Groups: PTEN$^{-/-}$ cells (5 mice for replicate (Rep.) A, 6 mice for Rep. B), *PTEN*$^{-/-}$ 50%: wild-type (WT) 50% (5 mice for Rep. A, 6 mice for Rep. B), *PTEN*$^{-/-}$10%: WT 90% (4 mice for Rep. A, 6 mice for Rep. B), WT 50%: WT 50% (5 mice for Rep. A, 6 mice for Rep. B).

(K) Ratio of GFP to mCherry in NCI-H82 cells *in vitro* and *in vivo* at day 25. Mixes are 10:90 and 50:50 mixes for *PTEN*$^{-/-}$ (GFP):WT (mCherry) and 10:90 for WT (GFP):WT (mCherry). See also Figures S6 and S7.

increased tumor growth in NJH29 but no growth advantage for NCI-H82 xenografts. Many biological observations are recapitulated in the two SCLC models. For instance, the same phenotypic clusters are detected in wild-type cells in both models, and there were increased patch sizes, higher percentages of non-NE cells, and phenotypic cluster mixing in the same patch in the *PTEN*$^{-/-}$ cell population in both models. EpicMIBI provided unique insights into the mechanisms underlying the *in vivo* growth differences between NCI-H82 and NJH29 *PTEN* knockout cells: there was a higher percentage of NE H3K27ac^{low} cells in the *PTEN*$^{-/-}$ NCI-H82 population, a strong compartmentalization of NE H3K27ac^{low} cells within the NCI-H82 xenografts, and an increased patch size on *PTEN* wild-type cells mixed with *PTEN*$^{-/-}$ NCI-H82 cells.

DISCUSSION

Clonal evolution is a major determinant of tumorigenesis. By applying a strategy for *in situ* tracking of barcodes in SCLC xenografts, we show that barcode-based multiplexing integrated with single-cell, deep *in-situ* tissue characterization can reveal new insights into tumor architecture and evolution. Our data show that even well-established cell lines can form complex tumor structures with inter-dependencies wherein one or more phenotypic states prefer or generate nearby distinct phenotypic states. Within these structures, we identified localized growth of clonal patches and detected distinct spatial dynamics of cell phenotypes within the tumor. We further extended the capabilities of the system by linking barcode expression to specific genome edits, opening new opportunities to study, *in situ*, complex autonomous and non-autonomous cellular effects during tumor growth.

The NCI-H82 and NJH29 cell lines were useful models to characterize and benchmark EpicMIBI, and this report exemplifies some of the biological insights that can be gained from these models. However, these cell line-based models are not fully representative of real tumor dynamics or cancer cell phenotypic heterogeneity as the immune system is absent, and certain clonal spatial dynamics might be biased. Expanding EpicMIBI to genetically modified mouse models and patient-derived xenografts will provide additional insights into tumor clonality, including cancer cell interactions with immune cell populations. This study is focused on how *PTEN* loss impacts spatial tumor heterogeneity. Other alterations in SCLC (George et al., 2015) with greater clinical and biological significance and additional SCLC subtypes (Rudin et al., 2019) could be similarly investigated by tagging edited cell lines and using more advanced *in vivo* models. EpicMIBI could be applied to study other cancer types to evaluate clonal patch behaviors across cancer types in tumor progression and response to therapy.

EpicMIBI is constrained by the number of barcodes deployed, the size and quality of the antibody panel, acquisition area, and debarcoding fidelity. Expanding the panel with additional antibodies targeting phenotypic, hypoxic, or cell death markers may generate new hypotheses about how certain cancer cell processes and protein functions shape the tumor microenvironment. MIBI is applicable to 2D tissue sections, limiting preservation of relevant clonal cell spatial interactions in the z axis, such as irregularly shaped tumor patches and vascular growth. The lack of information in the z dimension may be the reason for some of the observed "breaks" in connectivity of a clone, highlighting the need for 3D imaging. An appealing future direction is leveraging on technologies for 3D multiplex imaging, such as STARmap (Wang et al., 2018) or clearing-enhanced 3D microscopy (Li et al. 2017). In addition, multi-omics integration of EpicMIBI datasets with transcript-level information will provide a deeper understanding on tumor patch behavior (Zhu et al., 2021; Palla et al., 2022). The debarcoding pipeline also has limitations. Cells surrounded by other cells with different barcodes, cells with low barcode expression, and untagged cells are more prone to artifacts. In addition, signal spillover from neighboring cells may be a confounding factor; the application of a correction method similar to REDSEA (Bai et al., 2021) and machine learning approaches (Moen et al., 2019) are promising approaches to improve debarcoding.

In summary, the ability to track barcoded cancer cells *in situ*, together with the characterization of their spatial surroundings, opens new avenues for understanding tumor evolution. Leveraging the capability to trace complex populations at the subcellular level with distinct sets of genetic modifications, future work will be able to identify causal relations of genotypes and phenotypes to cellular neighborhoods and inter- and multiclone behaviors. Recently, Perturb-map, a combination of spatial epitope barcoding and spatial transcriptomics, has demonstrated an increase in the ability to identify regulators of the tumor microenvironment (Dhainaut et al., 2022). Spatial barcode tracing is a blooming technology uniquely positioned to reveal the spatiotemporal dynamics of tissues at the single-cell scale (reviewed in [Wagner and Klein 2020]); yet, major technical hurdles limit widespread availability. The refinement of EpicMIBI, Perturb-map, and other similar technologies (Frieda et al., 2017; Askary et al., 2020; Chow et al., 2021; Kudo et al. 2022; Zhao et al., 2022; Dhainaut et al., 2022) will help reveal principles and mechanisms of tissue developmental processes, in both normal and malignant growth, which will thus accelerate therapeutic discoveries.

STAR★METHODS

Detailed methods are provided in the online version of this paper and include the following:

- KEY RESOURCES TABLE
- RESOURCE AVAILABILITY
  - Lead contact
  - Materials availability
  - Data and code availability
- METHOD DETAILS
  - Cell line model
  - Xenograft mouse model
  - Vectors
  - Lentiviral production
  - Ribonucleoprotein nucleofection
  - Competition assays
  - Flow cytometry and cell sorting
  - Antibody conjugation to isotopes
  - Palladium barcoding for CyTOF
  - Cell preparation for CyTOF

- Tumor preparation for CyTOF
- Cell pellet preparation for MIBI
- Immunohistochemistry and immunofluorescence
- Tumor preparation for MIBI
- Gold-coated glass slide preparation
- Vectabond treatment of gold-coated slides
- Sample preparation for MIBI
- MIBI data acquisition
- Alpha MIBI
- Production MIBI
- Initial processing of MIBI images
- Cell segmentation of MIBI images
- Cell type annotation
- Cellular neighborhood analysis
- Debarcoding pipeline
- Patch enrichment analysis
- Statistical analysis
- Data visualization

SUPPLEMENTAL INFORMATION

Supplemental information can be found online at https://doi.org/10.1016/j.ccell.2022.09.014.

ACKNOWLEDGMENTS

We thank Dr. Maria Angulo-Ibáñez, Dr. Pablo Domizi, Pauline Chu, Catherine, Cheng Pan, Carswell-Crumpton, Alyssa Ray, Nicole Wang, Thuyen Nguyen, Angelica Trejo, Stanford's animal mouse facility staff, and all the members of the Jiang, Angelo, Bassik, Sage, and Nolan labs and previous and current members of IonPath Inc. for their help throughout the study. Research was supported by the EMBO postdoctoral fellowship (ALTF*300-2017; to X.R.-C.), the Tobacco-Related Disease Research Program (T30FT0824; to A.P.D.), the Stanford Dean's Fellowship and the Leukemia & Lymphoma Society CDP (to S.J.); Stanford Graduate Fellowship in Science and Engineering (to M.C.L.); grants of the National Institute of Health CA217450, and CA231997 (to J.S.), and 3U54HG010426, 5U54CA209971, 3U19AI100627, 5U2CCA233195, U19AI057229, 1U2CCA233238 (to G.P.N.); grant of the Food and Drug Administration HHSF223201610018C (to G.P.N.); grant of the Cancer Research UK C27165/A29073 (to G.P.N.); grant of the Bill and Melinda Gates Foundation OPP1113682 (to G.P.N.); grant of the Cancer Research Institute (to G.P.N.); grant of the Parker Institute for Cancer Immunotherapy (to G.P.N.); grant of the Kenneth Rainin Foundation 2018-575 (to G.P.N.); Celgene, Inc. 133826 and 134073 (to G.P.N.); the Rachford & Carlotta A. Harris Endowed Chair (to G.P.N.).

AUTHOR CONTRIBUTIONS

Conceptualization, X.R.-C., A.P.D., J.S., and G.P.N.; methodology, A.P.D. and X.R.-C.; software: S.J., X.R.-C., and A.P.D.; formal analysis, X.R.-C., A.P.D., S.J., and Y.B.; investigation, X.R.-C., A.P.D., S.J., J.S., and G.P.N.; novel reagents and tools, M.B., B.Z., A.E.D., M.C.L., T.P.C., A.H., R.A., E.F.M., N.F.G., M.M., and G.L.C.; writing – original draft, X.R.-C., A.P.D., J.S., and G.P.N.; writing – reviewing & editing, all authors; visualization, X.R.-C., A.P.D., S.J., J.S., and G.P.N.; supervision, M.A., M.C.B., J.S., and G.P.N.; project administration, J.S. and G.P.N.; funding acquisition, J.S. and G.P.N. X.R.-C., A.P.D., and S.J. contributed equally and have the right to list their name first in their CV.

DECLARATION OF INTERESTS

J.S. has equity in, and is an advisor for, DISCO Pharmaceuticals. G.P.N. and M.A. are co-founders and stockholders of Ionpath, Inc., and inventors on MIBI patents. The other authors declare no competing interests.

INCLUSION AND DIVERSITY

We support inclusive, diverse, and equitable conduct of research.

Received: May 29, 2021
Revised: July 22, 2022
Accepted: September 21, 2022
Published: October 13, 2022

REFERENCES

Angelo, M., Bendall, S.C., Finck, R., Hale, M.B., Hitzman, C., Borowsky, A.D., Levenson, R.M., Lowe, J.B., Liu, S.D., Zhao, S., et al. (2014). Multiplexed ion beam imaging of human breast tumors. Nat. Med. *20*, 436–442.

Askary, A., Sanchez-Guardado, L., Linton, J.M., Chadly, D.M., Budde, M.W., Cai, L., Lois, C., Elowitz, M.B., Cai, L., Lois, C., and Elowitz, M.B. (2020). "In situ readout of DNA barcodes and single base edits facilitated by in vitro transcription. Nat. Biotechnol. *38*, 66–75.

Bai, Y., Zhu, B., Rovira-Clave, X., Chen, H., Markovic, M., Chan, C.N., Su, T.-H., McIlwain, D.R., Estes, J.D., Keren, L., et al. (2021). Adjacent cell marker lateral spillover compensation and reinforcement for multiplexed images. Front. Immunol. *12*, 652631.

Baranski, A., Milo, I., Greenbaum, S., Oliveria, J.-P., Mrdjen, D., Angelo, M., and Keren, L. (2021). MAUI (MBI analysis user interface)-an image processing pipeline for multiplexed mass based imaging. PLoS Comput. Biol. *17*, e1008887.

Boone, P.G., Rochelle, L.K., Ginzel, J.D., Lubkov, V., Roberts, W.L., Nicholls, P.J., Bock, C., Flowers, M.L., von Furstenberg, R.J., Stripp, B.R., et al. (2019). A cancer rainbow mouse for visualizing the functional genomics of oncogenic clonal expansion. Nat. Commun. *10*, 5490.

Bowling, S., Sritharan, D., Osorio, F.G., Nguyen, M., Cheung, P., Rodriguez-Fraticelli, A., Patel, S., Yuan, W.C., Fujiwara, Y., Li, B.E., et al. (2020). An engineered CRISPR-cas9 mouse line for simultaneous readout of lineage histories and gene expression Profiles in single cells. Cell *181*, 1693–1694.

Chen, A., Liao, S., Cheng, M., Ma, K., Wu, L., Lai, Y., Qiu, X., Yang, J., Xu, J., Hao, S., et al. (2022). Spatiotemporal transcriptomic atlas of mouse organogenesis using DNA nanoball-Patterned arrays. Cell *185*, 1777–1792.e21.

Chow, K.-H.K., Budde, M.W., Granados, A.A., Cabrera, M., Yoon, S., Cho, S., Huang, T.-H., Koulena, N., Frieda, K.L., Cai, L., et al. (2021). Imaging cell lineage with a synthetic digital recording system. Science *372*, eabb3099.

Cui, M., Augert, A., Rongione, M., Conkrite, K., Parazzoli, S., Nikitin, A.Y., Ingolia, N., and MacPherson, D. (2014). PTEN is a potent suppressor of small cell lung cancer. Mol. Cancer Res. *12*, 654–659.

Dhainaut, M., Rose, S.A., Akturk, G., Wroblewska, A., Nielsen, S.R., Park, E.S., Buckup, M., Roudko, V., Pia, L., Sweeney, R., et al. (2022). Spatial CRISPR genomics identifies regulators of the tumor microenvironment. Cell *185*, 1223–1239.e20.

Easwaran, H., Tsai, H.-C., and Baylin, S.B. (2014). Cancer epigenetics: tumor heterogeneity, Plasticity of stem-like states, and Drug resistance. Mol. Cell *54*, 716–727.

Eng, C.H.L., Lawson, M., Zhu, Q., Dries, R., Koulena, N., Takei, Y., Yun, J., Cronin, C., Karp, C., Yuan, G.C., and Cai, L. (2019). Transcriptome-scale super-resolved imaging in tissues by RNA SeqFISH. Nature *568*, 235–239.

Frieda, K.L., Linton, J.M., Hormoz, S., Choi, J., Chow, K.-H.K., Singer, Z.S., Budde, M.W., Elowitz, M.B., and Cai, L. (2017). Synthetic recording and in situ readout of lineage information in single cells. Nature *541*, 107–111.

Gay, C.M., Stewart, C.A., Park, E.M., Diao, L., Groves, S.M., Heeke, S., Nabet, B.Y., Fujimoto, J., Solis, L.M., Lu, W., et al. (2021). Patterns of transcription factor Programs and immune Pathway activation define four major subtypes of SCLC with distinct therapeutic vulnerabilities. Cancer Cell *39*, 346–360.e7.

George, J., Lim, J.S., Jang, S.J., Cun, Y., Ozretić, L., Kong, G., Leenders, F., Lu, X., Fernández-Cuesta, L., Bosco, G., et al. (2015). Comprehensive genomic Profiles of small cell lung cancer. Nature *524*, 47–53.

Giesen, C., Wang, H.A.O., Schapiro, D., Zivanovic, N., Jacobs, A., Hattendorf, B., Schüffler, P.J., Grolimund, D., Buhmann, J.M., Brandt, S., et al. (2014).

Highly multiplexed imaging of tumor tissues with subcellular resolution by mass cytometry. Nat. Methods *11*, 417–422.

Goltsev, Y., Samusik, N., Kennedy-Darling, J., Bhate, S., Hale, M., Vazquez, G., Black, S., and Nolan, G.P. (2018). Deep Profiling of mouse splenic architecture with CODEX multiplexed imaging. Cell *174*, 968–981.e15.

Greenwald, N.F., Miller, G., Moen, E., Kong, A., Kagel, A., Dougherty, T., Fullaway, C.C., McIntosh, B.J., Leow, K.X., Schwartz, M.S., and et al. (2022). Whole-cell segmentation of tissue images with human-level performance using large-scale data annotation and deep learning. Nat. Biotechnol. *40*, 555–565.

Groves, S.M., Ildefonso, G.V., McAtee, C.O., Ozawa, P.M.M., Ireland, A.S., Stauffer, P.E., Wasdin, P.T., Huang, X., Qiao, Y., Lim, J.S., et al. (2022). Archetype tasks link intratumoral heterogeneity to Plasticity and cancer hallmarks in small cell lung cancer. Cell Syst. *13*, 690–710.e17. https://doi.org/10.1016/j.cels.2022.07.006.

Han, G., Spitzer, M.H., Bendall, S.C., Fantl, W.J., and Nolan, G.P. (2018). Metal-isotope-tagged monoclonal antibodies for high-dimensional mass cytometry. Nat. Protoc. *13*, 2121–2148.

Hanahan, D., and Weinberg, R.A. (2011). Hallmarks of cancer: the next generation. Cell *144*, 646–674.

Ireland, A.S., Micinski, A.M., Kastner, D.W., Guo, B., Wait, S.J., Spainhower, K.B., Conley, C.C., Chen, O.S., Guthrie, M.R., Soltero, D., et al. (2020). MYC drives temporal evolution of small cell lung cancer subtypes by reprogramming neuroendocrine fate. Cancer Cell *38*, 60–78.e12.

Jahchan, N.S., Dudley, J.T., Mazur, P.K., Flores, N., Yang, D., Palmerton, A., Zmoos, A.-F., Vaka, D., Tran, K.Q.T., Zhou, M., et al. (2013). A Drug repositioning approach identifies tricyclic antidepressants as inhibitors of small cell lung cancer and other neuroendocrine tumors. Cancer Discov. *3*, 1364–1377.

Jamal-Hanjani, M., Quezada, S.A., Larkin, J., and Swanton, C. (2015). Translational implications of tumor heterogeneity. Clin. Cancer Res. *21*, 1258–1266.

Ji, A.L., Rubin, A.J., Thrane, K., Jiang, S., Reynolds, D.L., Meyers, R.M., Guo, M.G., George, B.M., Mollbrink, A., Bergenstråhle, J., et al. (2020). Multimodal analysis of composition and spatial architecture in human squamous cell carcinoma. Cell *182*, 1661–1662.

Kalhor, R., Kalhor, K., Mejia, L., Leeper, K., Graveline, A., Mali, P., and Church, G.M. (2018). Developmental barcoding of whole mouse via homing CRISPR. Science *361*, eaat9804.

Keren, L., Bosse, M., Marquez, D., Angoshtari, R., Jain, S., Varma, S., Yang, S.-R., Kurian, A., Van Valen, D., West, R., et al. (2018). A structured tumor-immune microenvironment in triple negative breast cancer revealed by multiplexed ion beam imaging. Cell *174*, 1373–1387.e19.

Keren, L., Bosse, M., Thompson, S., Risom, T., Vijayaragavan, K., McCaffrey, E., Marquez, D., Angoshtari, R., Greenwald, N.F., Fienberg, H., et al. (2019). MIBI-TOF: a multiplexed imaging Platform relates cellular phenotypes and tissue structure. Sci. Adv. *5*, eaax5851.

Kudo, T., Lane, K., and Covert, M.W. (2022). A multiplexed epitope barcoding strategy that enables dynamic cellular phenotypic screens. Cell Syst. *13*, 376–387.e8.

Li, W., Germain, R.N., and Gerner, M.Y. (2017). Multiplex, quantitative cellular analysis in large tissue volumes with clearing-enhanced 3D microscopy (Ce3D). Proc. Natl. Acad. Sci. USA *114*, E7321–E7330.

Lim, J.S., Ibaseta, A., Fischer, M.M., Cancilla, B., O'Young, G., Cristea, S., Luca, V.C., Yang, D., Jahchan, N.S., Hamard, C., et al. (2017). Intratumoural heterogeneity generated by notch signalling promotes small-cell lung cancer. Nature *545*, 360–364.

Liu, Y., Yang, M., Deng, Y., Su, G., Enninful, A., Guo, C.C., Tebaldi, T., Zhang, D., Kim, D., Bai, Z., et al. (2020). High-spatial-resolution multi-omics sequencing via deterministic barcoding in tissue. Cell *183*, 1665–1681.e18. https://doi.org/10.1016/j.cell.2020.10.026.

McFadden, D.G., Papagiannakopoulos, T., Taylor-Weiner, A., Stewart, C., Carter, S.L., Cibulskis, K., Bhutkar, A., McKenna, A., Dooley, A., Vernon, A., et al. (2014). Genetic and clonal dissection of murine small cell lung carcinoma progression by genome sequencing. Cell *156*, 1298–1311.

McInnes, L., Healy, J., and James, M. (2018). UMAP: Uniform Manifold Approximation and Projection for Dimension Reduction. Preprint at arXiv. http://arxiv.org/abs/1802.03426.

Miller, I., Min, M., Yang, C., Tian, C., Gookin, S., Carter, D., and Spencer, S.L. (2018). Ki67 is a graded rather than a binary marker of proliferation versus quiescence. Cell Rep. *24*, 1105–1112.e5.

Moen, E., Bannon, D., Kudo, T., Graf, W., Covert, M., and Van Valen, D. (2019). Deep learning for cellular image analysis. Nat. Methods *16*, 1233–1246.

Palla, G., Spitzer, H., Klein, M., Fischer, D., Schaar, A.C., Kuemmerle, L.B., Rybakov, S., Ibarra, I.L., Holmberg, O., Virshup, I., et al. (2022). Squidpy: a scalable framework for spatial omics analysis. Nat. Methods *19*, 171–178.

Quinn, J.J., Jones, M.G., Okimoto, R.A., Nanjo, S., Chan, M.M., Yosef, N., Bivona, T.G., and Weissman, J.S. (2021). Single-cell lineages reveal the rates, routes, and drivers of metastasis in cancer xenografts. Science *371*, eabc1944.

Rodriques, S.G., Stickels, R.R., Goeva, A., Martin, C.A., Murray, E., Vanderburg, C.R., Welch, J., Chen, L.M., Chen, F., and Macosko, E.Z. (2019). Slide-seq: a scalable technology for measuring genome-wide expression at high spatial resolution. Science *363*, 1463–1467.

Rudin, C.M., Poirier, J.T., Byers, L.A., Dive, C., Dowlati, A., George, J., Heymach, J.V., Johnson, J.E., Lehman, J.M., MacPherson, D., et al. (2019). Molecular subtypes of small cell lung cancer: a synthesis of human and mouse model data. Nat. Rev. Cancer *19*, 289–297.

Schürch, C.M., Bhate, S.S., Barlow, G.L., Phillips, D.J., Noti, L., Zlobec, I., Chu, P., Black, S., Demeter, J., McIlwain, D.R., et al. (2020). Coordinated cellular neighborhoods orchestrate antitumoral immunity at the colorectal cancer invasive front. Cell *182*, 1341–1359.e19.

Shue, Y.T., Drainas, A.P., Li, N.Y., Pearsall, S.M., Morgan, D., Sinnott-Armstrong, N., Hipkins, S.Q., Coles, G.L., Lim, J.S., Oro, A.E., et al. (2022). A conserved YAP/notch/REST network controls the neuroendocrine cell fate in the lungs. Nat. Commun. *13*, 2690.

Shue, Y.T., Lim, J.S., Sage, J., and Sage, J. (2018). Tumor heterogeneity in small cell lung cancer defined and investigated in pre-clinical mouse models. Transl. Lung Cancer Res. *7*, 21–31.

Simpson, K.L., Stoney, R., Frese, K.K., Simms, N., Rowe, W., Pearce, S.P., Humphrey, S., Booth, L., Morgan, D., Dynowski, M., et al. (2020). A biobank of small cell lung cancer CDX models elucidates inter- and intratumoral phenotypic heterogeneity. Nat. Cancer *1*, 437–451.

Stewart, C.A., Gay, C.M., Xi, Y., Sivajothi, S., Sivakamasundari, V., Fujimoto, J., Bolisetty, M., Hartsfield, P.M., Balasubramaniyan, V., Chalishazar, M.D., et al. (2020). Single-cell analyses reveal increased intratumoral heterogeneity after the onset of therapy resistance in small-cell lung cancer. Nat. Cancer *1*, 423–436.

Tlemsani, C., Pongor, L., Elloumi, F., Girard, L., Huffman, K.E., Roper, N., Varma, S., Luna, A., Rajapakse, V.N., Sebastian, R., et al. (2020). SCLC-CellMiner: a resource for small cell lung cancer cell line genomics and Pharmacology based on genomic signatures. Cell Rep. *33*, 108296.

Van Gassen, S., Callebaut, B., Van Helden, M.J., Lambrecht, B.N., Demeester, P., Dhaene, T., and Saeys, Y. (2015). FlowSOM: using self-organizing maps for visualization and interpretation of cytometry data. Cytometry A. *87*, 636–645.

Van Valen, D.A., Kudo, T., Lane, K.M., Macklin, D.N., Covert, M.W., Macklin Quach, N.T., DeFelice, M.M., Maayan, I., Tanouchi, Y., and Ashley, E.A. (2016). Deep learning automates the quantitative analysis of individual cells in live-cell imaging experiments. PLoS Comput. Biol. *12*, e1005177.

Wagner, D.E., and Klein, A.M. (2020). Lineage tracing meets single-cell omics: opportunities and challenges. Nat. Rev. Genet. *21*, 410–427.

Wang, X., Allen, W.E., Wright, M.A., Sylwestrak, E.L., Samusik, N., Vesuna, S., Evans, K., Liu, C., Ramakrishnan, C., Liu, J., et al. (2018). Three-dimensional intact-tissue sequencing of single-cell transcriptional states. Science (New York, N.Y.) *361*, eaat5691. https://doi.org/10.1126/science.aat5691.

Wilkinson, L. (2011). Ggplot2: elegant graphics for data analysis by WICKHAM, H. Biometrics *67*, 678–679.

Wroblewska, A., Dhainaut, M., Ben-Zvi, B., Rose, S.A., Park, E.S., Amir, E.A.D., Bektesevic, A., Baccarini, A., Merad, M., Rahman, A.H., and Brown, B.D. (2018). Protein barcodes enable high-dimensional single-cell CRISPR screens. Cell *175*, 1141–1155.e16.

Zahir, N., Sun, R., Gallahan, D., Gatenby, R.A., and Curtis, C. (2020). Characterizing the ecological and evolutionary dynamics of cancer. Nat. Genet. *52*, 759–767.

Zhao, T., Chiang, Z.D., Morriss, J.W., LaFave, L.M., Murray, E.M., Del Priore, I., Meli, K., Lareau, C.A., Nadaf, N.M., Li, J., et al. (2022). Spatial genomics enables multi-modal study of clonal heterogeneity in tissues. Nature *601*, 85–91.

Zhu, B., Chen, S., Bai, Y., Chen, H., Mukherjee, N., Vazquez, G., McIlwain, D.R., Tzankov, A., Lee, I.T., Matter, M.S., et al. (2021). Robust single-cell matching and multi-modal analysis using shared and distinct features reveals orchestrated immune responses. Preprint at bioRxiv. https://doi.org/10.1101/2021.12.03.471185.

STAR★METHODS

KEY RESOURCES TABLE

REAGENT or RESOURCE	SOURCE	IDENTIFIER
Antibodies		
Vimentin (D21H3) XP® Rabbit	Cell Signaling Technology	Cat# 5741S; RRID: AB_10695459
Histone H3 (D1H2) XP	Cell Signaling Technology	Cat# 4499S; RRID: AB_10544537
Histone H3 Phospho (Ser28)	BioLegend	Cat# 641002; RRID: AB_1227659
Mitochondria	Abcam	Cat# ab92824; RRID: AB_10562769
Ki-67	Cell Signaling Technology	Cat# 9449; RRID: AB_2797703
α-Smooth Muscle Actin	Cell Signaling Technology	Cat# 19245; RRID: AB_2734735
CD31	Abcam	Cat# ab225883
Citrate Synthase	Abcam	Cat# ab129095
GLUT1	Abcam	Cat# ab115730; RRID: AB_2832207
H2AX (pS139), γH2AX	BD Biosciences	Cat# 560443; RRID: AB_1645592
Synaptophysin	Novus	Cat# NBP1-47483; RRID: AB_10010435
H3K27ac	Thermo Fisher Scientific	Cat# MA5-23516; RRID: AB_2608307
H3K4me2	Thermo Fisher Scientific	Cat# 701764; RRID: AB_2532505
H4K8ac	Thermo Fisher Scientific	Cat# 701796; RRID: AB_2532510
mCherry	Abcam	Cat# ab167453; RRID: AB_2571870
GFP	Abcam	Cat# ab183735; RRID: AB_2732027
VSV-G Tag	Thermo Fisher Scientific	Cat# PA1-30138; RRID: AB_1961360
E2 Tag	GenScript	Cat# A00630; RRID: AB_914515
Strep Tag II	GenScript	Cat# A01732; RRID: AB_2622218
Protein C Tag	GenScript	Cat# A01774; RRID: AB_2744686
Tag-100 Tag	GenScript	Cat# A00677; RRID: AB_915550
AU1 Tag	Bethyl	Cat# A190-124A; RRID: AB_155848
FLAG Tag	Millipore-Sigma	Cat# F1804; RRID: AB_262044
HA Tag	Thermo Fisher Scientific	Cat# 26183; RRID: AB_10978021
Cleaved caspase 3	BD Biosciences	Cat# 559565; RRID: AB_397274
NEUROD1	Abcam	Cat# ab109224; RRID: AB_10861489
YAP1	Cell Signaling Technology	Cat# 14074; RRID: AB_2650491
NOTCH2	Cell Signaling Technology	Cat#5732; RRID: AB_10693319
Hexokinase-1	Abcam	Cat# ab150423; RRID: N/A
H4K12ac	Thermo Fisher Scientific	Cat# 712991; RRID: AB_2895909
Na^+ K^+ ATPase	Abcam	Cat# ab167390; RRID: AB_2890241
H3K4me1	Thermo Fisher Scientific	Cat# 710795; RRID: AB_2532764
ATP5A	Abcam	Cat# ab14748; RRID: AB_301447
CD56	Ionpath	Cat# 715101-100; RRID: AB_2861293
H4K20me1	Thermo Fisher Scientific	Cat# MA5-18067; RRID: AB_2539450
SLC1A5 / ASCT2	Abcam	Cat# ab251591; RRID: N/A
CD107a (LAMP-1)	BioLegend	Cat# 328602; RRID: AB_1134259
H3K9ac	Cell Signaling Technology	Cat# 9649; RRID: AB_823528
H3K27me3	Cell Signaling Technology	Cat# 9733; RRID: AB_2616029
ImmPRESS HRP Horse anti-Rabbit IgG	Vector Labs	MP-7801-15
Alexa Fluor 594 Donkey anti-Goat IgG	Thermo Fisher Scientific	Cat# A-11058; RRID: AB_2534105
Alexa Fluor 488 Donkey anti-Rabbit IgG	Thermo Fisher Scientific	Cat# A-21206, RRID: AB_2535792
Bacterial and virus strains		
Endura™ Chemically Competent Cells	Lucigen	Cat# 60240-1

(*Continued on next page*)

Continued

REAGENT or RESOURCE	SOURCE	IDENTIFIER
Chemicals, peptides, and recombinant proteins		
Alt-R® S.p. Cas9	Integrated DNA Technologies	Cat# 1081059
Polyethylenimine (PEI)	Polysciences	Cat# 23966-1
Polybrene	Millipore-Sigma	Cat# TR-1003-G
Opti-MEM	Thermo Fisher Scientific	Cat# 31985088
RPMI 1640	Corning	Cat# 15-040-CV
DMEM	Thermo Fisher Scientific	Cat# 11965092
Bovine Growth Serum	Thermo Fisher Scientific	Cat# SH3054103HI
Penicillin-Streptomycin-Glutamine	Thermo Fisher Scientific	Cat# 10378016
Fetal Bovine Serum	Thermo Fisher Scientific	Cat#16000044
Matrigel	BD biosciences	Cat# 356237
Tris(2-carboxyethyl) phosphine hydrochloride (TCEP)	Thermo Fisher Scientific	Cat# 77720
PBS antibody stabilizer	Thermo Fisher Scientific	Cat# NC0414486
Paraformaldehyde (PFA)	Thermo Fisher Scientific	Cat# 28906
Saponin	Millipore-Sigma	Cat# S7900-100G
Bovine Serum Albumin (BSA)	Millipore-Sigma	Cat# A3059
Sodium azide	Millipore-Sigma	Cat# 71289
Cell-ID Intercalator-Ir	Fluidigm	Cat# 201192B
L15 media	Millipore-Sigma	Cat# L1518
Collagenase I	Millipore-Sigma	Cat# C0130
Collagenase II	Millipore-Sigma	Cat# 6885
Collagenase IV	Millipore-Sigma	Cat# 5138
Elastase	CellSystems	Cat# LS002292
DNAseI	Millipore-Sigma	Cat# 10104159
RBC Lysis Buffer	Thermo Fisher Scientific	Cat# 00-4333-57
Histogel	Thermo Fisher Scientific	Cat# NC9150318
Vectabond	Vector Labs	Cat# SP-1800-7
1X Dako Target Retrieval Solution	Agilent	Cat# S2375
1X TBS IHC wash buffer with Tween 20	Cell Marque	Cat# 935B-09
Donkey serum	Millipore-Sigma	Cat# D9663-10ML
Triton X-100	Millipore-Sigma	Cat# T8787-100ML
Glutaraldehyde	Electron Microscopy Sciences	Cat# 16120
H-3300	Vector Labs	Cat# H-3300-250
DAB reagent	Vector Labs	Cat# SK-4100
Hematoxylin	Millipore-Sigma	Cat# HHS32
Refrax Mounting Medium	Anatech Ltd	Cat# 711
Fluoromount-G	SouthernBiotech	Cat# 0100-01
Histo-Clear II	National Diagnostics	Cat# HS-202
Hydrogen peroxide	VWR	Cat# BP2633-500
Horse serum	Thermo Fisher	Cat# 16050-130
Critical commercial assays		
SE Cell Line 4D-NucleofectorTM X Kit S	Lonza	Cat# V4XC-1032
Herculase II Fusion DNA Polymerase kit	Agilent	Cat# 600675
Maxpar X8 polymers	Fluidigm	Cat# 201300
Cell-ID™ 20-Plex Pd Barcoding Kit	Fluidigm	Cat# 201060
TSA Plus Fluorescein kit	Akoya Biosciences	Cat# NEL741001KT
Deposited data		
Source data for datasets 1 to 3 and the code for debarcoding	Mendeley Data	https://data.mendeley.com/datasets/4y3fzctgxn/draft?a=042a495e-998a-4caf-b967-4030b7f5e7bf

(*Continued on next page*)

Continued

REAGENT or RESOURCE	SOURCE	IDENTIFIER
Experimental models: Cell lines		
293T	ATCC®	HTB-3216™
NCI-H82	ATCC®	HTB-175™
NJH29	Sage Lab	N/A
NCI-H82-epicTAG-GFP-VSVg-StrepTagII-ProtC	This paper	N/A
NCI-H82-epicTAG- GFP-VSVg-StrepTagII-HA	This paper	N/A
NCI-H82-epicTAG- GFP-VSVg-StrepTagII-FLAG	This paper	N/A
NCI-H82-epicTAG- GFP-VSVg-StrepTagII-AU1	This paper	N/A
NCI-H82-epicTAG- GFP-VSVg-ProtC-HA	This paper	N/A
NCI-H82-epicTAG- GFP-VSVg-ProtC-FLAG	This paper	N/A
NCI-H82-epicTAG- GFP-VSVg-ProtC-AU1	This paper	N/A
NCI-H82-epicTAG- GFP-VSVg-HA-FLAG	This paper	N/A
NCI-H82-epicTAG- GFP-VSVg-HA-AU1	This paper	N/A
NCI-H82-epicTAG- GFP-VSVg-FLAG-AU1	This paper	N/A
NCI-H82-epicTAG- GFP-StrepTagII-ProtC-HA	This paper	N/A
NCI-H82-epicTAG- GFP-StrepTagII-ProtC-FLAG	This paper	N/A
NCI-H82-epicTAG- GFP-StrepTagII-ProtC-AU1	This paper	N/A
NCI-H82-epicTAG- GFP-StrepTagII-HA-FLAG	This paper	N/A
NCI-H82-epicTAG- GFP-StrepTagII-HA-AU1	This paper	N/A
NCI-H82-epicTAG- GFP-StrepTagII-FLAG-AU1	This paper	N/A
NCI-H82-epicTAG- GFP-ProtC-HA-FLAG	This paper	N/A
NCI-H82-epicTAG- GFP-ProtC-HA-AU1	This paper	N/A
NCI-H82-epicTAG- GFP-ProtC-FLAG-AU1	This paper	N/A
NCI-H82-epicTAG- GFP-HA-FLAG-AU1	This paper	N/A
NCI-H82-epicTAG-mCherry-VSVg-StrepTagII-ProtC	This paper	N/A
NCI-H82-epicTAG- mCherry -VSVg-StrepTagII-HA	This paper	N/A
NCI-H82-epicTAG- mCherry -VSVg-StrepTagII-FLAG	This paper	N/A
NCI-H82-epicTAG- mCherry -VSVg-StrepTagII-AU1	This paper	N/A
NCI-H82-epicTAG- mCherry -VSVg-ProtC-HA	This paper	N/A
NCI-H82-epicTAG- mCherry -VSVg-ProtC-FLAG	This paper	N/A
NCI-H82-epicTAG- mCherry -VSVg-ProtC-AU1	This paper	N/A
NCI-H82-epicTAG- mCherry -VSVg-HA-FLAG	This paper	N/A
NCI-H82-epicTAG- mCherry -VSVg-HA-AU1	This paper	N/A
NCI-H82-epicTAG- mCherry -VSVg-FLAG-AU1	This paper	N/A
NCI-H82-epicTAG- mCherry -StrepTagII-ProtC-HA	This paper	N/A
NCI-H82-epicTAG- mCherry -StrepTagII-ProtC-FLAG	This paper	N/A
NCI-H82-epicTAG- mCherry -StrepTagII-ProtC-AU1	This paper	N/A
NCI-H82-epicTAG- mCherry -StrepTagII-HA-FLAG	This paper	N/A
NCI-H82-epicTAG- mCherry -StrepTagII-HA-AU1	This paper	N/A
NCI-H82-epicTAG- mCherry -StrepTagII-FLAG-AU1	This paper	N/A
NCI-H82-epicTAG- mCherry -ProtC-HA-FLAG	This paper	N/A
NCI-H82-epicTAG- mCherry -ProtC-HA-AU1	This paper	N/A
NCI-H82-epicTAG- mCherry -ProtC-FLAG-AU1	This paper	N/A
NCI-H82-epicTAG- mCherry -HA-FLAG-AU1	This paper	N/A

(*Continued on next page*)

Continued

REAGENT or RESOURCE	SOURCE	IDENTIFIER
NJH29-epicTAG-GFP-VSVg-StrepTagII-ProtC	This paper	N/A
NJH29-epicTAG- GFP-VSVg-StrepTagII-HA	This paper	N/A
NJH29-epicTAG- GFP-VSVg-StrepTagII-FLAG	This paper	N/A
NJH29-epicTAG- GFP-VSVg-StrepTagII-AU1	This paper	N/A
NJH29-epicTAG- GFP-VSVg-ProtC-HA	This paper	N/A
NJH29-epicTAG- GFP-VSVg-ProtC-FLAG	This paper	N/A
NJH29-epicTAG- GFP-VSVg-ProtC-AU1	This paper	N/A
NJH29-epicTAG- GFP-VSVg-HA-FLAG	This paper	N/A
NJH29-epicTAG- GFP-VSVg-HA-AU1	This paper	N/A
NJH29-epicTAG- GFP-VSVg-FLAG-AU1	This paper	N/A
NJH29-epicTAG- GFP-StrepTagII-ProtC-HA	This paper	N/A
NJH29-epicTAG- GFP-StrepTagII-ProtC-FLAG	This paper	N/A
NJH29-epicTAG- GFP-StrepTagII-ProtC-AU1	This paper	N/A
NJH29-epicTAG- GFP-StrepTagII-HA-FLAG	This paper	N/A
NJH29-epicTAG- GFP-StrepTagII-HA-AU1	This paper	N/A
NJH29-epicTAG- GFP-StrepTagII-FLAG-AU1	This paper	N/A
NJH29-epicTAG- GFP-ProtC-HA-FLAG	This paper	N/A
NJH29-epicTAG- GFP-ProtC-HA-AU1	This paper	N/A
NJH29-epicTAG- GFP-ProtC-FLAG-AU1	This paper	N/A
NJH29-epicTAG- GFP-HA-FLAG-AU1	This paper	N/A
NJH29-epicTAG- mCherry-ProtC-FLAG-AU1	This paper	N/A
NJH29-epicTAG- mCherry -HA-FLAG-AU1	This paper	N/A
Experimental models: Organisms/strains		
NOD-scid IL2Rgammanull mice (NSG mice)	The Jackson Laboratory	#005557
Oligonucleotides		
sgPTEN-1: GTGCATATTTATTACATCG	This paper	Synthego
sgPTEN-2: GAGGCCCTAGATTTCTATG	This paper	Synthego
sgPTEN-3: GATAAGTTCTAGCTGTGG	This paper	Synthego
sgSAFE-1: GATTAATTATGCAACCAGTA	This paper	Synthego
sgSAFE-2: GTGATGTGTGTGGCTTGGAT	This paper	Synthego
sgSAFE-3: GTTAGACTGCAAACACCCAC	This paper	Synthego
sgNON-TAR-A-1: GTGCGCGCATCATGCTACGA	This paper	Synthego
sgNON-TAR-A-2: GGGCCGTTATATGACGGT	This paper	Synthego
sgNON-TAR-A-3: GCGGAGCGTACCCGATTGGG	This paper	Synthego
sgNON-TAR-B-1: GTTTATCGCCCGTGGTCG	This paper	Synthego
sgNON-TAR-B-2: GTGCGGCGCATATCGAG	This paper	Synthego
sgNON-TAR-B-3: GGCTCGTACGCGCCCCTGT	This paper	Synthego
Recombinant DNA		
pEpicVector3G_Puro-T2A-EGFP-VSVg-StrepTagII-ProtC	This paper	Addgene: #162079
pEpicVector3G_Puro-T2A-EGFP-VSVg-StrepTagII-HA	This paper	Addgene: #162080
pEpicVector3G_Puro-T2A-EGFP-VSVg-StrepTagII-FLAG	This paper	Addgene: #162081
pEpicVector3G_Puro-T2A-EGFP-VSVg-StrepTagII-AU1	This paper	Addgene: #162082
pEpicVector3G_Puro-T2A-EGFP-VSVg-ProtC-HA	This paper	Addgene: #162083
pEpicVector3G_Puro-T2A-EGFP-VSVg-ProtC-FLAG	This paper	Addgene: #162084

(*Continued on next page*)

Continued

REAGENT or RESOURCE	SOURCE	IDENTIFIER
pEpicVector3G_Puro-T2A-EGFP-VSVg-ProtC-AU1	This paper	Addgene: #162085
pEpicVector3G_Puro-T2A-EGFP-VSVg-HA-FLAG	This paper	Addgene: #162086
pEpicVector3G_Puro-T2A-EGFP-VSVg-HA-AU1	This paper	Addgene: #162087
pEpicVector3G_Puro-T2A-EGFP-VSVg-FLAG-AU1	This paper	Addgene: #162088
pEpicVector3G_Puro-T2A-EGFP-StrepTagII-ProtC-HA	This paper	Addgene: #162089
pEpicVector3G_Puro-T2A-EGFP-StrepTagII-ProtC-FLAG	This paper	Addgene: #162090
pEpicVector3G_Puro-T2A-EGFP-StrepTagII-ProtC-AU1	This paper	Addgene: #162091
pEpicVector3G_Puro-T2A-EGFP-StrepTagII-HA-FLAG	This paper	Addgene: #162092
pEpicVector3G_Puro-T2A-EGFP-StrepTagII-HA-AU1	This paper	Addgene: #162093
pEpicVector3G_Puro-T2A-EGFP-StrepTagII-FLAG-AU1	This paper	Addgene: #162094
pEpicVector3G_Puro-T2A-EGFP-ProtC-HA-FLAG	This paper	Addgene: #162095
pEpicVector3G_Puro-T2A-EGFP-ProtC-HA-AU1	This paper	Addgene: #162096
pEpicVector3G_Puro-T2A-EGFP-ProtC-FLAG-AU1	This paper	Addgene: #162097
pEpicVector3G_Puro-T2A-EGFP-HA-FLAG-AU1	This paper	Addgene: #162098
pEpicVector3mC_Puro-T2A-mCherry-VSVg-StrepTagII-ProtC	This paper	Addgene: #162099
pEpicVector3mC_Puro-T2A-mCherry-VSVg-StrepTagII-HA	This paper	Addgene: #162100
pEpicVector3mC_Puro-T2A-mCherry-VSVg-StrepTagII-FLAG	This paper	Addgene: #162101
pEpicVector3mC_Puro-T2A-mCherry-VSVg-StrepTagII-AU1	This paper	Addgene: #162102
pEpicVector3mC_Puro-T2A-mCherry-VSVg-ProtC-HA	This paper	Addgene: #162103
pEpicVector3mC_Puro-T2A-mCherry-VSVg-ProtC-FLAG	This paper	Addgene: #162104
pEpicVector3mC_Puro-T2A-mCherry-VSVg-ProtC-AU1	This paper	Addgene: #162105
pEpicVector3mC_Puro-T2A-mCherry-VSVg-HA-FLAG	This paper	Addgene: #162106
pEpicVector3mC_Puro-T2A-mCherry-VSVg-HA-AU1	This paper	Addgene: #162107
pEpicVector3mC_Puro-T2A-mCherry-VSVg-FLAG-AU1	This paper	Addgene: #162108
pEpicVector3mC_Puro-T2A-mCherry-StrepTagII-ProtC-HA	This paper	Addgene: #162109
pEpicVector3mC_Puro-T2A-mCherry-StrepTagII-ProtC-FLAG	This paper	Addgene: #162110
pEpicVector3mC_Puro-T2A-mCherry-StrepTagII-ProtC-AU1	This paper	Addgene: #162111
pEpicVector3mC_Puro-T2A-mCherry-StrepTagII-HA-FLAG	This paper	Addgene: #162112
pEpicVector3mC_Puro-T2A-mCherry-StrepTagII-HA-AU1	This paper	Addgene: #162113

(*Continued on next page*)

Continued

REAGENT or RESOURCE	SOURCE	IDENTIFIER
pEpicVector3mC_Puro-T2A-mCherry-StrepTagII-FLAG-AU1	This paper	Addgene: #162114
pEpicVector3mC_Puro-T2A-mCherry-ProtC-HA-FLAG	This paper	Addgene: #162115
pEpicVector3mC_Puro-T2A-mCherry-ProtC-HA-AU1	This paper	Addgene: #162116
pEpicVector3mC_Puro-T2A-mCherry-ProtC-FLAG-AU1	This paper	Addgene: #162117
pEpicVector3mC_Puro-T2A-mCherry-HA-FLAG-AU1	This paper	Addgene: #162118
pRSV-Rev	Addgene	Addgene: #12253
pMDLg/pRRE	Addgene	Addgene: #12251
pCI-VSVG	Addgene	Addgene: #1733
Software and algorithms		
ImageJ	Schneider et al., 2012	https://imagej.nih.gov/ij/
R	R Core Team (2020)	https://www.R-project.org/
Custom debarcoding algorithm	This paper	N/A
CellEngine	CellCarta	https://cellcarta.com/
Cytobank	Cytobank	https://cytobank.org/
Other		
0.22 μm filter	Millipore-Sigma	Cat# SLMP025SS
70 μm strainer	Fisher Scientific	Cat# 08-771-2
Superfrost Plus glass slides of 25 mm width and 75 mm length	Thermo Fisher Scientific	Cat#12-550-15
PAP pen	Vector Laboratories	Cat# H-4000
Lonza 4D-NucleofectorTM X Unit	Lonza	AAF-1002X
Linear stainer	Leica	Cat# ST4020
PT module	Thermo Fisher Scientific	Cat# A80400012
CytoFLEX Flow Cytometer	Beckman Coulter	https://www.beckman.com/flow-cytometry/instruments/cytoflex
BD FACSAria™ III Cell Sorter	BD Biosciences	https://www.bdbiosciences.com/en-us/instruments/research- instruments/research-cell-sorters/facsaria- iii
CyTOF II Mass Cytometer	Fluidigm	https://www.fluidigm.com/products/helios
MIBI-TOF Mass Spectrometers (Alpha and Production)	IonPath	https://www.ionpath.com/mibiscope/

RESOURCE AVAILABILITY

Lead contact

Further information and requests for resources and reagents should be directed to and will be fulfilled by the Lead Contact: Garry P. Nolan, gpnolan@stanford.edu.

Materials availability

Plasmids generated in this study have been deposited to Addgene (Deposit 78,757).

Data and code availability

Three datasets were acquired in this study. Datasets were named "Batch 3" (related to Figures 3–5 and S3–S5), "Batch 6" (related to Figures 6 and S6), and "Batch 7" (related to Figure S7). Metadata that includes the number of mice, tumors, and regions acquired per dataset is available in Table S1. Single-cell information for each dataset is available in Tables S2–S4. The metadata in Table S1 can be paired to the sheets named "SummaryMatrix.csv" of Table S2 by the columns named "tile_ID" and "file_name". Source data for

datasets 1 to 3 and the code for debarcoding is available at Mendeley Data: https://data.mendeley.com/datasets/4y3fzctgxn/draft?a=042a495e-998a-4caf-b967-4030b7f5e7bf.

METHOD DETAILS

Cell line model

NCI-H82 cells were purchased from ATCC (HTB-175). NJH29 cells were developed at Stanford (Jahchan et al., 2013). Cells were cultured in RPMI media: RPMI 1640 (Corning, #15-040-CV) with 10% bovine growth serum (Thermo Fischer Scientific, #SH3054103HI), plus 1x penicillin/streptomycin plus glutamine (Thermo Fisher Scientific, #10378016). Cells tested negative for mycoplasma.

Xenograft mouse model

Mice were maintained according to practices prescribed by the NIH at Stanford's Research Animal Facility and by the Institutional Animal Care and Use Committee (IACUC, protocol 13,565) at Stanford. Additional accreditation of Stanford animal research facility was provided by the Association for Assessment and Accreditation of Laboratory Animal Care (AAALAC). All mice were housed in micro-isolator cages and sentinel mice were used for monitoring for pathogens. Single cell suspensions were prepared in antibiotic-free media and mixed with Matrigel (BD biosciences, # 356,237) at a 1:1 ratio. Aliquots of 200 μL (2-5 x 10^6 cells) were injected subcutaneously into the flanks of NOD-scid IL2Rgamma^{null} mice (NSG mice). Tumors were collected once they reached a size of ~1 cm^3. Following tumor induction, animals were monitored daily, including weekends and holidays, as recommended by the Guide for the Care and Use of Laboratory Animals. Animals were observed for pain, distress, and abnormal behavior and physiology. Any mouse with a tumor that ulcerated or inhibited limb movement was euthanized immediately.

Vectors

EpicVectors are lentiviral vectors that express a puromycin resistance gene, T2A, and GFP or mCherry linked to a combination of three of six possible epitopes (VSVg, AU1, FLAG, StrepII, Prot C, and HA). The vectors are deposited to Addgene (#162079-162118), and information available is in the Key Resources table.

Lentiviral production

One day prior to transfection, 293T cells (ATCC, CRL-3216) were seeded in DMEM (Thermo Fisher Scientific, #11965092) and 10% fetal bovine serum (Thermo Fisher Scientific, # 16,000,044) at 10^6 cells per well of a 6-well plate. The following day, 293T cells were transfected with a mixture of 0.5 μg of each lentiviral EpicVector (Key Resources), 0.5 μg of third generation lentiviral vectors (at a 1:1:1 ratio of VSV-g, pMDLg/pRRE, and pRSV-Rev), 5 μL PEI (Polysciences, #23966-1) in 50 μL Opti-MEM (Thermo Fisher Scientific, # 31,985,088). The mixture was incubated 10 min and added dropwise to cells. The next day, the media was removed, and 2 mL of fresh antibiotic-free media was added to the cells. After 2 days, all viruses were collected, and cells were infected with 2 mL of virus per 4x10^6 cells for each EpicVector, with the addition of polybrene (Millipore-Sigma, #TR-1003-G) at 8 μg/mL, bringing the total volume of media to 5 mL. The next day, the virus was removed, and fresh media containing penicillin/streptomycin (Thermo Fisher Scientific, #10378016) was added. After 2 days, MOI was measured by FACS for GFP or mCherry. Puromycin was added for approximately 1 week until over 98% of cells were positive for GFP or mCherry.

Ribonucleoprotein nucleofection

Three sgRNAs were designed to hybridize approximately 150 bases apart on the target of interest (see Key Resources) and were synthesized by Synthego. The three sgRNAs were resuspended in Tris-EDTA and were mixed at a 1:1:1 ratio. First, 12 μL of SE buffer (Lonza, #V4XC-1032) was added to each well of a 96-well v-bottom plate. Then 3 μL of sgRNA (300 pmol for all three sgRNAs) was added to the SE buffer. An aliquot of 0.5 μL of Alt-R S.p. Cas9 (Integrated DNA Technologies, # 1,081,059) was added to 10 μL of SE buffer. Next the Cas9 was added to the sgRNA solution, mixed thoroughly, and incubated at 37°C for 15 min to form the ribonucleoproteins (RNPs). NCI-H82 and NJH29 cells were pelleted, counted, and resuspended to 10^6 cells per reaction in 5 μL of SE Buffer. Cells and the RNP solution were added to each well. Cells were immediately nucleofected using the Lonza 4D-Nucleofector X Unit (Lonza, #AAF-1002X) with the EN150 program. After nucleofection, warm RPMI media was added to the cells. Cells were incubated at 37°C for 15 min and then transferred to a 24-well plate. Editing efficiency was evaluated 4 days later by FACS or sequencing.

Competition assays

NCI-H82 and NJH29 expressing EpicTag vectors (GFP-VSVg-StrepTagII-ProtC and GFP-VSVg-StrepTagII-HA) were subjected to PTEN inactivation via ribonucleoprotein nucleofection. Controls NCI-H82 and NJH29 cells expressing mCherry EpicTag vectors (mCherry-ProtC-FLAG-AU1, mCherry-HA-FLAG-AU1) were mixed with *PTEN*$^{-/-}$ cells in specific ratios: 10% GFP-*PTEN*$^{-/-}$:90% mCherry-WT cells or 50% GPF-PTEN−/−:50% mCherry-WT or 10% GPF-WT:90% mCherry-WT. Cells were then cultured *in vitro* or injected subcutaneously in the flanks of NSG mice. Cells were collected from *in vitro* and *in vivo* when the tumors reached ~1 cm^3. GFP and mCherry expressing cells were analyzed by flow cytometry.

Flow cytometry and cell sorting

Flow cytometry was conducted on a CytoFLEX (Beckman Coulter) and on a FACSAria (BD Biosciences). Analysis of the data was done using Cytobank and R analysis software.

Antibody conjugation to isotopes

The antibodies listed in the Key Resources Table were conjugated to isotope-chelated Maxpar X8 polymers (Fluidigm, #201300) as previously described (Han et al., 2018). Briefly, 100 μg of antibody in carrier-free PBS were partially reduced by TCEP treatment (Thermo Fisher Scientific, #77720) for 30 min at 37°C. Reduced-antibodies were mixed with isotope-chelated polymers for 1.5 h at 37°C. Antibody concentration was quantified via Nanodrop. Isotope-conjugated antibodies were diluted to >0.2 mg/mL in PBS antibody stabilizer (Thermo Fisher Scientific, #NC0414486) and stored at 4°C.

Palladium barcoding for CyTOF

Cells were fixed in freshly prepared 1.6% Paraformaldehyde (PFA) in 1X PBS (Thermo Fisher Scientific, #28906) for 20 min at room temperature. Cells were washed twice with ice-cold 1X PBS and once with ice-cold 0.02% Saponin (Millipore-Sigma, #S7900-100G) in 1X PBS for 20 min at 4°C. Each palladium barcode (Fluidigm, #201060) was resuspended in 1 mL ice-cold 0.02% Saponin in 1X PBS and transferred to the selected sample. Cells were pipetted to ensure proper mixing with the palladium barcoding reagent and incubated for 15 min at room temperature. Cells were then washed twice with cell staining media (CSM; 0.5% BSA (Millipore-Sigma, #A3059) and 0.02% sodium azide (Millipore-Sigma, #71289) in 1X PBS), and mixed into a single cell suspension.

Cell preparation for CyTOF

Cells were fixed in freshly prepared 1.6% PFA in 1X for 20 min at room temperature. Cells were washed thrice with cold 1X PBS and permeabilized in pre-chilled 100% methanol for 20 min at 4°C. Cells were washed once with 1X PBS and twice with CSM. Barcoded cells were stained for 3 h at 4°C in CSM with the following cocktail of isotope-conjugated antibodies at 2 μg/mL: anti-GFP, anti-AU1, anti-FLAG, anti-HA, anti-StrepII, anti-Prot C, anti-VSVg, and anti-cleaved caspase 3 (clone C92-605, BD Biosciences, #559565). After staining, cells were washed twice with CSM, once with 1X PBS, and incubated with 1X PBS containing 1.6% PFA and 1 μM iridium-based DNA intercalator (Fluidigm, #201192B) for 16 h at 4°C. After intercalation, cells were washed once with 1X PBS and thrice with distilled water before analysis. Data were collected with a CyTOF II mass cytometer (Fluidigm). The raw FCS files processing was performed in CellEngine (CellCarta) by gating out doublets based on cell length, debris based on iridium staining, and dead cell based on cleaved caspase staining. The resulting data were plotted using UMAP (*umap* R package v.0.2.7.0) (McInnes et al. 2018) and visually inspected to identify barcodes.

Tumor preparation for CyTOF

Tumors were collected from the flanks of the mice and were minced using a razor blade. The samples were then placed to a 50 mL conical tube containing 9 mL of L15 media (Sigma Aldrich, #L1518) plus 1 mL enzyme mix (10 mL L15 with 85 mg Collagenase I (Millipore-Sigma, #C0130), 28 mg Collagenase II (Millipore-Sigma, # 6885), 85 mg Collagenase IV (Millipore-Sigma, # 5138), 12.5 mg Elastase (CellSystems, # LS002292), 12.5 mg DNAseI (Millipore-Sigma, #10104159) and filtered with a 0.22 μm filter (Millipore-Sigma, # SLMP025SS)). The samples were incubated at 37°C for 15 min in a slant with rotation. Then the mixture was filtered using a 70 μm strainer (Fisher Scientific, # 08-771-2) into a new 50 mL tube. The samples were centrifuged at 400 xg for 5 min at room temperature. The supernatant was discarded, and 1 mL of red blood cell lysis buffer (Thermo Fisher Scientific, Cat# 00-4333-57) was added for 30 s. Then, 30 mL of 1XPBS were added and the samples were centrifuged at 400 g for 5 min at room temperature. Cells were collected in RPMI media without antibiotics supplemented with 10% DMSO, and frozen down to −80°C until use.

Cell pellet preparation for MIBI

All 20 barcoded NCI-H82 cell lines were mixed in a 15 mL conical tube and washed twice in cold 1X PBS by centrifuging at 125 xg for 5 min at 4°C. The supernatant was decanted, 10 mL of freshly prepared 4% PFA in 1X PBS was carefully placed on top of the pellet, and the tube was placed on a rocker set at low speed for 16 h at 4°C. The PFA-fixed cell pellet was pressed with a tip to cast it loose from the bottom of the tube and rinsed thrice by pouring and decanting 10 mL 1X PBS. The pellet was briefly dried on top of an absorbent piece of paper, transferred to a new 15 mL conical tube, submerged in pre-heated Histogel (Thermo Fisher Scientific, #NC9150318), and incubated for 10 min at 4°C. The Histogel-embedded pellet was placed in a 9-spaces chamber, submerged in 80% ethanol, and FFPE processed.

Immunohistochemistry and immunofluorescence

Paraffin sections were rehydrated with serial immersion in Histo-Clear (National Diagnostics, #HS-202), 100% ethanol, 95% ethanol, 70% ethanol, and water for 5 min each. For antigen retrieval, rehydrated sections were immersed in citrate-based antigen unmasking solution (Vector Laboratories, #H-3300-250) at boiling temperature for 15 min. Slides were then incubated in 3% hydrogen peroxide (VWR, #BP2633-500) for 1 h, washed in PBS-T (PBS +0.1% Tween 20), blocked using blocking buffer (5% horse serum (Thermo Fisher, #16050-130) in PBS-T) for 1 h at room temperature, and incubated overnight with primary antibodies at 4°C. Sections were then washed with PBS-T, incubated with secondary antibodies for 1 h at room temperature, and either developed using

DAB reagent for immunohistochemistry (Vector Laboratories, #SK-4100) or stained with 0.6 nM DAPI in PBS for 10 min at room temperature for immunofluorescence following PBS-T washes. For immunohistochemistry, slides were then counterstained with hematoxylin (Millipore-Sigma, #HHS32), dehydrated with 70% ethanol, 100% ethanol, and xylene immersions, and mounted with Refrax Mounting Medium (Anatech Ltd, #711). For immunofluorescence, slides were mounted with Fluoromount-G (SouthernBiotech, #0100-01) and stored in 4°C overnight or −20°C for a few days prior to visualization. For YAP1, signals were amplified using TSA Plus Fluorescein kit (Akoya Biosciences, #NEL741001KT).

The following antibodies and kits were used: anti-NEUROD1 (Abcam, #ab109224, 1:200), anti-YAP1 (CST, #14074S, 1:200), anti-NOTCH2 (CST, #5732, 1:400) ImmPRESS HRP Horse anti-Rabbit IgG (Vector Laboratories, #MP-7801-15).

Tumor preparation for MIBI

Tumors were collected immediately after euthanasia, submerged in 10 mL of freshly prepared 4% PFA in 1X PBS (Thermo Fisher Scientific, #28906), and placed on a rocker set at low speed for 24 h at room temperature. Tumors were then rinsed thrice with 1X PBS, transferred to 80% ethanol, and FFPE processed.

Gold-coated glass slide preparation

Superfrost Plus glass slides of 25 mm width and 75 mm length (Thermo Fisher Scientific, #12-550-15) were soaked in dish detergent, rinsed twice with distilled water, soaked in acetone, and air-dried with compressed air in a fume hood. Clean slides were coated with a 30 nm tantalum layer followed by a 100 nm gold layer. Coating was prepared at the Stanford Nano Shared Facility (Stanford, CA) and New Wave Thin Films (Newark, CA) as previously described (Ji et al., 2020; Keren et al., 2019).

Vectabond treatment of gold-coated slides

Gold-coated slides were silanized by Vectabond treatment (Vector labs, #SP-1800-7). Using glass beakers, gold-coated slides were submerged in acetone for 5 min, placed in freshly prepared Vectabond solution (3.5 mL Vectabond and 175 mL acetone) for 30 min, and air-dried with compressed air in a fume hood. Slides were baked at 70°C for 30 min and stored at room temperature.

Sample preparation for MIBI

FFPE blocks were sectioned using a microtome into 5 μm thin sections and placed on vectabond-treated gold-coated slides. Tissue sections were baked for 20 min at 70°C, and immediately deparaffinized and rehydrated with fresh reagents as follows: xylene (x3), 100% ethanol (x2), 95% ethanol (x2), 80% ethanol, 70% ethanol, distilled water (x3). Each wash was performed for 3 min at room temperature with repetitive dipping using a linear stainer (Leica, #ST4020). Slides were transferred for heat-induced epitope retrieval to a PT module (Thermo Fisher Scientific, #A80400012) pre-heated to 75°C. Samples in 1X Dako Target Retrieval Solution, pH 9 (Agilent, #S2375) were heated to 97°C, stayed at the same temperature for 10 min, and then cooled down to 65°C.

Slides were washed twice with 1X TBS IHC wash buffer with Tween 20 (Cell Marque, #935B-09) and 0.1% BSA (Thermo Fisher Scientific, #BP1600-100) for 5 min at room temperature. A hydrophobic barrier around the tissue was drawn using a PAP pen (Vector Laboratories, #H-4000). Tissue sections were blocked in 1X TBS IHC wash buffer with Tween 20, 2% normal donkey serum (Millipore-Sigma, #D9663-10ML) (MIBI wash buffer), 0.1% Triton X-100 (Millipore-Sigma, #T8787-100ML), and 0.05% sodium azide (Millipore-Sigma, #71289-50G) for 1 h at room temperature. Tissue sections were then stained for 16 h at 4°C in 1X TBS IHC wash buffer with Tween 20, 3% normal donkey serum, and 0.05% sodium azide with the following cocktail of isotope-conjugated antibodies: anti-GFP, anti-AU1, anti-FLAG, anti-HA, anti-StrepII, anti-Prot C, anti-VSVg, anti-Vimentin, anti-HH3, anti-phosphoS28 HH3, anti-human-specific mitochondrial marker, anti-Ki-67, anti-αSMA, anti-CD31, anti-Citrate synthase, anti-GLUT1, anti-phosphoS139H2AX (γH2AX), anti-synaptophysin, anti-H3K27ac, anti-H3K4me2, and anti-H4K8ac.

After staining, slides were washed thrice with MIBI wash buffer for 5 min at room temperature, post-fixed with a solution of 2% glutaraldehyde (Electron Microscopy Sciences, #16120) and 4% PFA in 1X PBS for 5 min at room temperature and quenched with 100mM Tris pH 7.5 for 5 min at room temperature. Tissue sections were then dehydrated with fresh reagents as follows: 100mM Tris pH 7.5 (x2), distilled water (x3), 70% ethanol, 80% ethanol, 95% ethanol (x2), 100% ethanol (x2). Each wash was performed for 3 min at room temperature with repetitive dipping using a linear stainer. The slides were air-dried and stored at room temperature under vacuum until MIBI acquisition.

MIBI data acquisition

We acquired three datasets for this study. Datasets 1 and 2 consist of NCI-H82 xenografts, and dataset 3 consists of NJH29 xenografts. Dataset 1, also named Batch 3, consists of the 16 tiles used for Figures 3–5 and S3–S5. Dataset 2, also named Batch 6, consists of 14 tiles, 4 ''Control'' and 10 ''PTEN'', used for Figures 6 and S6. Tile 13 of batch 6 consists of eight FOVs. Dataset 3, also named Batch 7, consists of 15 tiles, 7 ''Control'' and 8 ''PTEN'', used for Figure S7.

MIBI datasets 1 and 2 were acquired on a custom MIBI-TOF mass spectrometer, named Alpha MIBI, equipped with a duoplasmatron ion source running research grade oxygen (Airgas, OX R80). MIBI dataset 3 was acquired on a commercially available MIBIscope™ System (IonPath), named Production MIBI, equipped with a xenon ion source. Each tile acquired consisted of 9 FOV (Figure S3C). The acquisition parameters per FOV were the following:

Alpha MIBI

- Pixel dwell time: 7 ms
- Image area: 400 × 400 μm
- Image size: 512 x 512 pixels
- Probe size: ~ 400 nm
- Primary ion current: ~ 3.5 nA
- Number of depths: 1 depth

Production MIBI

- Pixel dwell time: 1 ms
- Image area: 400 × 400 μm
- Image size: 1024 x 1024 pixels
- Probe size: ~ 400 nm
- Primary ion current: ~ 5 nA
- Number of depths: 1 depth

Initial processing of MIBI images

Raw MIBI data from datasets 1 and 2 were processed using MIBIAnalysis tools (https://github.com/lkeren/MIBIAnalysis) as previously described (Baranski et al., 2021; Keren et al., 2018). The mass spectra were calibrated using sodium and gold, and background was subtracted using the gold channel. Raw MIBI data from dataset 3 was processed using toffy (https://github.com/angelolab/toffy), background and signal contamination were removed and channel crosstalk compensated by the Rosetta algorithm. The number of nearest neighborhoods for denoising of all datasets was 25. Image stitching and flat-field correction was performed using custom MATLAB scripts developed by Dmitry Tebaykin (https://github.com/dtebaykin/MibiStitch) and Sizun Jiang.

Cell segmentation of MIBI images

MIBI image cell segmentation was obtained with Mesmer, a deep learning algorithm based on the DeepCell library (deepcell-tf 0.6.0) (Van Valen et al., 2016; Greenwald et al., 2022). The neural network weights for prediction were imported from https://deepcell-data.s3-us-west-1.amazonaws.com/model-weights/Multiplex_Segmentation_20200908_2_head.h5. Segmentation was computed using denoised and capped at the 99.seventh percentile images of HH3 and human-specific mitochondrial marker as input, to account for the nucleus and cytoplasm, respectively. Model_mpp in the python script multiplex_segmentation.py was 1.8 for dataset 1, 1.6 for dataset 2, and 1.0 for dataset 3.

Cell type annotation

Cell segmentation was used to extract cell counts per marker. Counts were normalized by cell size, scaled based on the median HH3 expression per cell in each tile, and transformed using an inverse hyperbolic sine (asinh) with cofactor of 0.05 (to account for the adjustment based on HH3 scaling).

Unsupervised single-cell clustering was performed using the FlowSOM R package (Van Gassen et al., 2015). The channels used for clustering were vimentin, pS28 HH3, human-specific mitochondrial marker, Ki-67, αSMA, CD31, citrate synthase, GLUT1, γH2AX, synaptophysin, H3K27ac, H3K4me2, and H4K8ac. Phenotypic SOM clusters were manually annotated based on visual inspection of the heatmap of marker expression per SOM cluster. Multiplex MIBI images were carefully compared to the SOM cluster maps, generated by coloring the cells with the respective SOM cluster, to assess accuracy and specificity of the clustering result and annotation. Single-cells were plotted using the umap R package (n_neighbors = 15 and min_dist = 0.01) and colored by SOM cluster to orthogonally inspect the clustering results and annotation. Single cells in properly annotated clusters were classified, and the remainder clusters were subjected to additional rounds of clustering until all cells were annotated. A post-clustering identification of endothelial cells was performed by selecting cells with low human-specific mitochondrial marker, small cell size, and high CD31 expression.

Cellular neighborhood analysis

Cell centroids were computed and the 30 nearest neighbors were selected for each cell. The frequencies of each SOM cluster were calculated per cell. Data from all tiles for each dataset were combined, and CNS were selected using k-means (k = 20) and labeled based on visual inspection of the heatmap of SOM cluster frequencies per CN. The CN maps were generated by coloring the cells with the respective CN.

Debarcoding pipeline

Epitope debarcoding was performed by merging cell-based and pixel-based barcode assignment. The input for cell-based assignment of barcodes were the segmentation map and the six epitope MIBI images. Epitope counts within each segmented cell were extracted, normalized, and ordered to provide a barcode (1–20) to each cell.

The input for pixel-based assignment of barcodes were the six epitope MIBI images. A sliding window scan was applied to extract the counts of each epitope by centering an n x n window to each pixel. The size of the sliding window was an odd number (e.g., 3 x 3, 5 x 5, etc.). After applying a sliding window, the value of each epitope was capped at the 95th percentile, and a barcode (1–20) was provided based on the 3 most expressed epitopes. A selection step of the third minus the fourth most expressed epitopes being higher than 0.05 was applied to account for blank pixels. The data were plotted back to the 2D tissue space and groups of pixels larger than 30 and sharing a barcode were selected. The unselected pixels were subjected to extra rounds of scanning with sliding window of larger size, up to sliding windows of 11 x 11.

To merge cell- and pixel-based barcode assignments, each cell within the tile is classified in one of six categories.

- Category a: a cell with the same cell-based barcode as its pixel-based barcode retains that barcode.
- Category b: a cell with a cell-based barcode without pixel-based barcode is assigned the cell-based barcode.
- Category c: a cell without a cell-based barcode without pixel-based barcode results in a cell without barcode.
- Category d: a cell without a cell-based barcode that has 50% or more of its area within an area of the same pixel-based barcode is assigned the pixel-based barcode.
- Category e: A cell with cell-based barcode within areas with two or more pixel-based barcodes results in a cell with the barcode of the area from which the cell shares the highest surface percentage.
- Category f: A cell with cell-based barcode overlapping with an area presenting a distinct pixel-based barcode results in a cell keeping the cell-based barcode if the percentage of shared area is less than 50%. Alternatively, it results in a cell with pixel-based barcode if the percentage of shared area is 50% or more.

To identify clonal tumor patches, a barcode based on the merging step was provided to pixels related to single cells, and a barcode from the pixel-based barcode assignment was provided to pixels unrelated to single cells. Single cells within groups of pixels sharing a barcode were provided with the same patch identification number.

The debarcoding pipeline is schematically depicted in Figure 4: (1a) Epitope images are the input for pixel-based assignment of barcodes. (1b) A sliding window approach is applied to obtain a pixel-based assignment of barcodes. The cyan region within the dashed red circle in the enlarged image exemplifies a large region of the tumor sharing the same barcode. (2a) HH3 and human cell marker images are the initial inputs for cell-based assignment of barcodes. (2b) Single cells are segmented using Mesmer. (2c) Segmentation maps (step 2b) and epitope images (step 1a) are merged to obtain a cell-based assignment of barcodes. Epitope counts within each segmented region are extracted, normalized, and ordered to provide a barcode for each cell. Cyan cells within the dashed red circle in the enlarged image show that cells within the same patch (as shown in 1b) are not in direct contact after segmentation. (3) Merging step for cell- and pixel-based barcode assignments. Patches are shown as irregular shapes. Single cells are shown as small circles. Both depicted patches are bigger than a single cell to exemplify than patches consist of a group of cells. Barcodes are shown as colors. A dashed circle indicates a cell without an assigned barcode. To merge cell- and pixel-based barcode assignments, each cell within the tile is classified in one of six merging categories. On each category, left indicates the results from cell- and pixel-based barcode assignments and right indicates the result after integration. (4a) A connectivity map is obtained for each tile. Each circle represents a cell. Gray lines indicate that cells not directly touching in the segmentation map are from the same patch. (4b) A barcode is provided to each cell, resulting in a collection of images (one for each of the 20 barcodes). (5) Together the connectivity map (4a) and the barcode readouts (4b) represent a clonal tumor map.

Patch enrichment analysis

For each clonal tumor map, a patch size map was created with pixels having a value of the patch size they belong, in pixels. Patch size was capped at 10 times the median of cell size, in pixels, in the entire dataset. A sliding window of 119 x 119 pixels was applied to the patch size map, summing values at each pass. The patch enrichments maps were generated by coloring the results of the sliding window to a continuous scale.

Statistical analysis

Statistical analysis was conducted using R. Significance is calculated by ANOVA within and between groups and adjusted by Bonferroni. P-adjusted: 0.05–0.01:*, 0.01–0.001:**, <0.001:***.

Data visualization

MIBI data visualization was performed in ImageJ or Ionpath MIBITracker. Plots were created using the ggplot2 R package (Wilkinson 2011). Figures 1, 2, 6A, and S2A were created in part using BioRender.com. All figures were prepared using Illustrator (Adobe).